

Ferri- and Ferro-Electric Switching in Spontaneously Chiral Polar Liquid Crystals

Jordan Hobbs^{1,*}, Calum J. Gibb², and Richard J. Mandle^{1,2}

¹*School of Physics & Astronomy, University of Leeds, UK and*

²*School of Chemistry, University of Leeds, UK*

(Dated: February 13, 2025)

The recent discovery of spontaneous chiral symmetry breaking has demonstrated the possibility of discovering the exotic textures of ferromagnetic systems in liquid crystalline fluid ferro-electrics. We show that the polar smectic mesophase exhibited by the first molecule discovered to exhibit a spontaneously chiral ferroelectric nematic phase is also helical has a strongly varied textural morphology depending in its thermal history and phase ordering. Electro-optic studies demonstrate that the two spontaneously chiral phases exhibit field induced phase transitions. For the nematic variant, this process is threshold-less and has no hysteresis while for the smectic it has a clear threshold and shows hysteresis meaning this phase exhibits pseudo-ferrielectric switching, the first of its kind for ferroelectric nematic like phases. We show that helix formation can be both 1st and 2nd order but when it is 1st it is accompanied by pre-transitional helix formation in the preceding ferroelectric nematic phase.

I. INTRODUCTION

Spontaneous symmetry breaking is a general phenomena where a symmetric system will undergo some transition to an asymmetric state where it is no longer invariant under some symmetry operation and has wide ranging consequences for the natural world such as homochirality in biology [1], autocatalysis in chemistry [2], the Higgs mechanism in physics [3] and even in the understanding of crowd control [4]. Liquid crystals can have various components of order (orientational, translational, bond orientation etc.) and, as such, symmetry breaking can have profound effects on the properties exhibited by the phase [5]. Ferroelectric liquid crystals are notable examples of symmetry breaking within soft matter research resulting in a variety of phase structures with distinctly different properties. Chiral smectic C liquid crystals (SmC*) form a tilted helical structure where the molecular ordering of dipole moments associated with the chiral centre break mirror symmetry resulting in an orthogonal polar phase that can be made ferroelectric upon proper confinement [6, 7]. Bent core liquid crystals can spontaneously break inversion symmetry forming phase structures containing layer polarisations of various types [8, 9] as well as also spontaneously breaking chiral symmetry where the layer polarisation rotates around a helix [10]. The twist bend nematic (N_{TB}) is another example of chiral symmetry breaking, forming a phase that has degenerate left and right handed heliconic molecular organisation resulting in a phase that is both chiral and locally polar [9, 11, 12].

In 2017, the ferroelectric nematic phase (N_F) phase was discovered [13–15] in which the molecules spontaneously align syn-parallel to each other thus breaking inversion symmetry and resulting in longitudinally polar phases [16–24]. It has been shown that the N_F phase can spon-

taneously break chiral symmetry to form π -twisted domains [25] to reduce the electrostatic cost of polarisation [22]. Further investigations into novel N_F materials led to the discovery of additional longitudinally polar phases [26–33] and two that showed not only broken inversion symmetry but also distinct spontaneously chiral heliconic molecular organisation [29, 34].

The so called ferroelectric twist bend nematic (N_{TBF}) phase [34, 35] (also referred to a $^{HC}N_F$ [36]) and polar helical smectic C (SmC_P^H) phase [29] both spontaneously form heliconic ordering of the LC molecules with a temperature dependent pitch around ~ 400 - 1000 nm resulting in selective reflection of visible light. Notably, below the N_{TBF} phase a further phase transition into a tilted smectic phase of unknown structure was observed [34]. This raises the question: does the helix unwind in some fashion to form a non helical ferroelectric SmC phase, as has been recently discovered [30–32], or does the helix remain meaning the phase is actually a SmC_P^H phase?

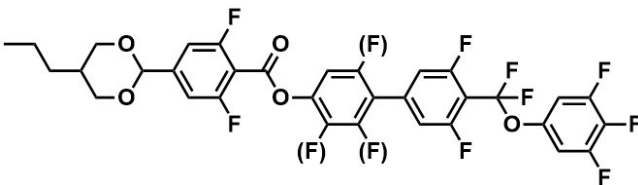

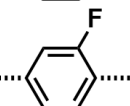
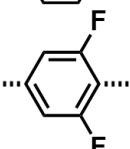
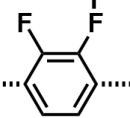
In this paper we demonstrate this to be the latter case, showing that this unknown smectic phase is a SmC_P^H phase (we will refer to the SmC_P^H phase in **2** briefly as SmC_F throughout the first section of this article) showing continual existence of the heliconic structure and that the texture and defects of the SmC_P^H phase varies strongly on the phase preceding it. We demonstrate that while both heliconic phases show a field induced phase transition into their non-helical and non-tilted counterparts, the SmC_P^H exhibits hysteresis of this behaviour indicating ferrielectric switching while the N_{TBF} does not. We also show that further transitions in the SmC_P^H phase are possible and that these are accompanied by pre-transitional helix formation.

II. MATERIALS

Table I shows the chemical structures and phases transitions of the materials presented here. Details of chemical synthesis and analysis (NMR, HPLC, HRMS) can

* j.l.hobbs@leeds.ac.uk

TABLE I. Transition temperatures (T) and associated enthalpies of transition (ΔH) for compounds 1–4 determined by DSC on cooling at a rate of $10^\circ\text{C min}^{-1}$.

											
No.		Melt	$\text{SmC}_P^H\text{-SmA}_F$	$\text{SmA}_F\text{-SmA}$	SmA-N	$\text{SmC}_P^H\text{-N}_F$	$\text{SmC}_P^H\text{-N}_{TBF}$	$\text{N}_{TBF}\text{-N}_F$	$\text{N}_F\text{-N}_S$	$\text{N}_S\text{-N}$	N-Iso
1		T ($^\circ\text{C}$)	100.9	90.1 ^a	129.7	154.3	-	-	-	-	225.6
		ΔH (kJ/mol)	31.1	-	0.6	0.1	-	-	-	-	1.0
2		T ($^\circ\text{C}$)	64.0	-	-	-	91.6	104.4 ^a	142.6	146.4	225.1
		ΔH (kJ/mol)	19.0	-	-	-	0.1	-	0.4	0.01	1.1
3		T ($^\circ\text{C}$)	93.8	-	-	-	90.6	-	178.4	179.5 ^a	213.7
		ΔH (kJ/mol)	19.2	-	-	-	0.6	-	0.7	-	1.3
4		T ($^\circ\text{C}$)	99.8	-	-	-	-	-	119.3	126.7	233.8
		ΔH (kJ/mol)	25.1	-	-	-	-	-	0.2	0.01	1.6

Note: ^a determined via POM observations as no corresponding peak was observed in DSC

be found in the ESI. All four compounds detailed here contain a 1,3-dioxane ring and so will show isomerisation from the equatorial trans state to the axial trans state just as for the classic ferroelectric mesogen DIO [37]. While for DIO this isomerisation will occur above $\sim 140^\circ\text{C}$ the increased size of the molecules here increases the energy barrier for the isomerisation to occur. Our experiments suggest that quickly heating to $\sim 150^\circ\text{C}$ does not result in a reduction in transition temperatures but sustained time above this temperature results in a reduction in all transition temperatures indicative of isomerisation. Compounds **1** [29] and **2** [34] have been characterised previously and so their characterisation via DSC, X-ray, and Ps measurements are included in the ESI while compounds **3** and **4** will be discussed in section VI.

III. POLARISED OPTICAL MICROSCOPY

Compound **1** melts into the SmA_F phase and in cells prepared with either parallel or anti-parallel rubbed surfaces forms blocky textures when viewed using polarised optical microscopy (POM) (**fig. S1a**). From azimuthal rotation of the cell with respect to the polarisers, it is clear that most of the blocky domains are orientated with the director close to the rubbing direction but with some slight in plane ϕ rotation diving the texture into domains. The blocky texture results from the restriction of splay deformations by the electrostatic cost of polarisation splay and the restriction of bend deformation by

the formation of layers [26, 38]. Heating into the SmA phase retains these domains (**fig. S1b**) but they are lost upon reaching the N phase where a uniform planar texture is obtained. Upon cooling back into the SmA_F phase a monodomain texture is obtained (**fig. S1c**) regardless of cell thickness. No evidence of director twist [22, 25] is found even in cells using parallel rubbed planar alignment layers.

Immediately upon transitioning to the SmC_P^H phase striations appear parallel to the rubbing direction with an average periodicity of around $1.2\ \mu\text{m}$ at 80°C (**fig. 1**). While the average periodicity of these striations is generally independent of cell thickness, the periodicity takes a greater possible range of values for increasing cell thickness. Upon cooling these striations behave quite differently depending on cell thicknesses. For thin cells ($1.6\ \mu\text{m}$) the striation periodicity decreases to around $0.8\ \mu\text{m}$ by crystallisation at around 55°C (**fig. 1a**). For thicker cells ($5\ \mu\text{m}$) the striations initially decrease in periodicity before larger less uniformly shaped striations grow in to become the dominant texture (**fig. 1b**). For $10\ \mu\text{m}$ thick cells the non-uniform striations grow into thick and distinct defect lines, though these do not have to encompass a full domain and do not show alternative optical activity upon slight de-crossing of the polarisers (**fig. 1c**). $20\ \mu\text{m}$ thick cells behave similarly to the $10\ \mu\text{m}$ thick cell except the temperature threshold for the defect lines is much closer to the $\text{SmA}_F\text{-SmC}_P^H$ transition (**fig. 1d**). These striations are clearly distinct from alternating polarisation domains [29] and form even when

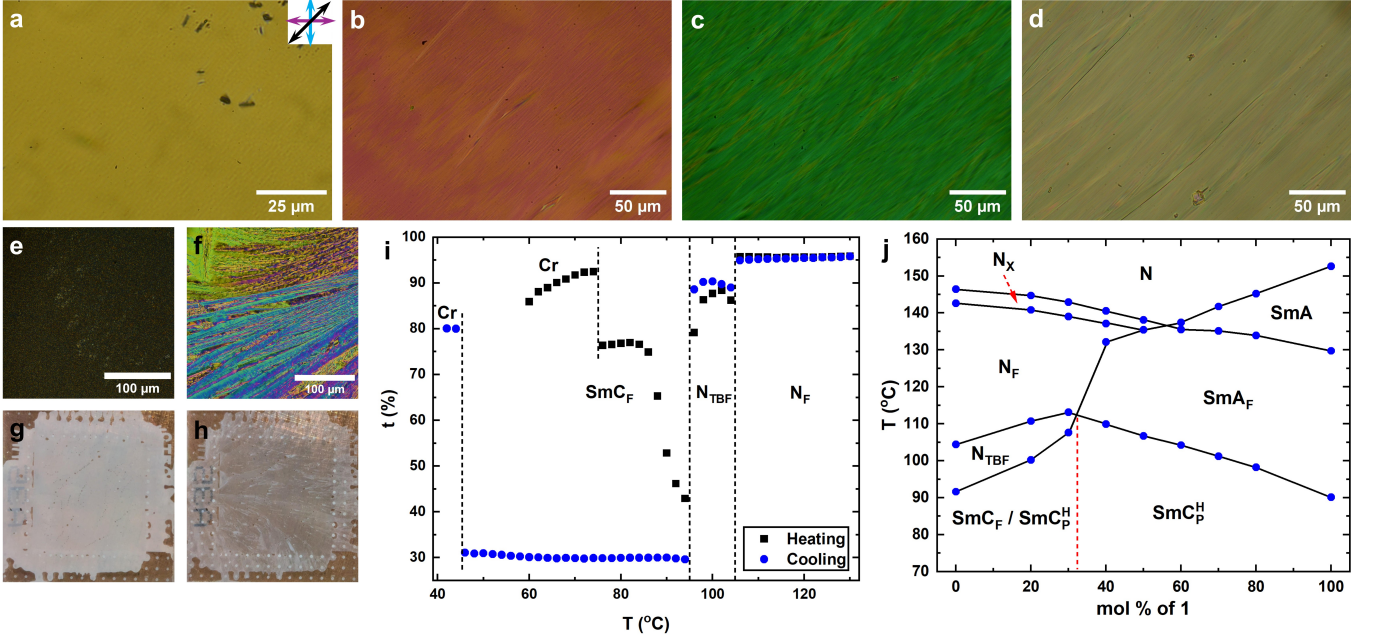


FIG. 1. POM images taken for compound **1** at 80 °C filled into parallel rubbed, planar aligned cells with a cell gap of **a)** 1.6 μm , **b)** 5 μm , **c)** 10 μm and **d)** 20 μm . POM images of **2** at 80 °C filled into parallel rubbed, planar aligned cell with a cell gap of 5 μm on **e)** heating directly after melting from the crystal phase and **f)** subsequent cooling after heating to the nematic phase. Corresponding macroscopic texture of an entire 4 μm cell filled with **2** at 80 °C on **g)** heating and **h)** cooling. The brown background colour comes from the hot stage plate. **i)** Transmission intensity of white light through a sample of **2** in a 5 μm thick planar aligned parallel rubbed cell. **j)** Binary phase diagram between **1** and **2** with 100 % compound **1** on the right and 100 % compound **2** on the left. The red vertical dashed line marks the point where the SmC_P^H phase switches polymorphism from the highly scattering to the striated as discussed in the text. For all POM images polarisor axis' and rubbing direction are marked by the blue, purple and black arrows respectively.

a monodomain SmA_F texture aligned under an in-plane electric field is cooled into the SmC_P^H phase. They are also retained upon applying a weak in-plane electric field parallel to the polarisation direction.

The smectic phase, SmC_F , exhibited by **2** shows quite different behaviour where in cells of 1.6 μm , 5 μm , 10 μm and 20 μm thickness the texture is consistently grainy and nondescript (**fig. 1e**) when the sample is cooled from the preceding N_{TB} phase resulting in significant light scattering and low light transmission though the cell (**fig. 1i**). The SmC_F phase in compound **2** is monotropic and the texture exhibited by the phase on melting directly from the crystal phase is distinctly different (**fig. 1f**). The melt texture is paramorphic of the crystal phase but does not show any of the defects and scattering found in the phase on cooling. On heating the melted SmC_F texture to ~ 10 °C below the transition into the N_{TB} the defects found on cooling begin to form and the transmission through the sample drops significantly but does decrease to the values obtained on cooling. While selective reflection is difficult to be observed on cooling a faint blue colour can be seen in the SmC_F phase with the naked eye on heating suggesting that this phase does retain the helical structure of the preceding N_{TB} phase.

If the SmC_F phase is helical than the differences in

optical textures on heating/cooling could result from the fact that the greatest change in pitch length (i.e. likely close to the phase transition) occurs in the same temperature regime as the scattering texture forms. These defects would then be the result of plastic deformation of the pitch though contraction and dilation [39]. However, so far the scattering texture have precluded optical measurement of any pitch length in the SmC_F phase. We also note that the scattering behaviour of **2** in the SmC_F phase is not isolated to cell confinement geometries and shows the same highly scattering and opaque appearance when filled into capillaries or as bulk samples in droplet form or in vials demonstrating that it is not a result of confinement.

IV. BINARY PHASE DIAGRAM BETWEEN **1** AND **2**

Construction of binary phase diagrams is a well established technique in liquid crystal science to demonstrate whether two materials possess the same phase by establishing miscibility between the two materials across the full phase diagram [40] and has been well applied to the N_F phase already [41]. Binary mixtures of **1** and **2**

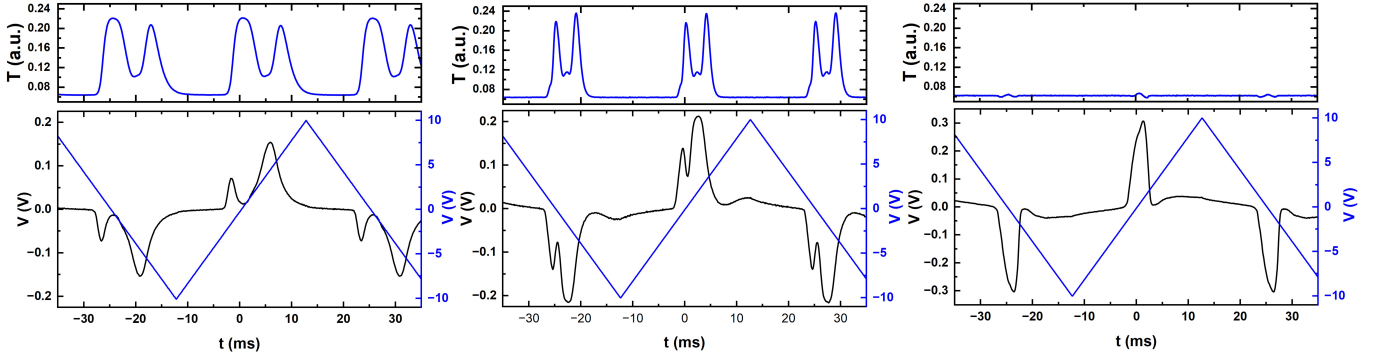


FIG. 2. Electro-optic and current response to an 20 Hz, 10 V_{RMS} applied triangle wave for **a)** compound 1 at 75°C, **b)** compound 2 at 75 °C and **c)** compound 2 at 99 °C. Each compound is filled into a 4 μm thick cell with bare ITO electrodes. The top portion of the graphs shows the transmission through the cell placed with between crossed polarisers as detected by a photo-diode while the bottom portion is the current response.

were created and the resulting phase diagram shown in **fig. 1j**. From the binary phase diagram of **1** and **2** the SmC_P^H phase is completely miscible with the SmC_F phase demonstrating that the SmC_F phase is heliconic that the two phases are structurally the same. The studies presented so far have shown the SmC_F found in **2** [34] is the same as the SmC_P^H phase reported by us [29] and so we shall refer to the SmC_F phase of **2** as a SmC_P^H phase from here on.

The apolar-polar transition temperature (whether this is $N-N_S$ or SmA-SmA_F) is roughly linear with concentration while the transition to helical order, whether this is nematic of smectic type, is actually stabilised with a peak at around 30 % of **1** for both the N_{TBF} and the SmC_P^H phase indicating that the molecular origins of ferroelectric order vs spontaneously chiral differ for these systems. It also points to the possibility of using mixtures in the future to construct systems with wide phase existence for application purposes. We note that the peak of chiral phase stability also roughly coincides with the point at which the transition pattern switches between N_F - N_{TBF} - SmC_P^H to SmA_F - SmC_P^H . It is also this point where the texture and scattering behaviour changes from the highly scattering uncharacteristic texture to the striated texture. Seemingly, the key difference is the fact that the SmC_F texture on cooling is from the N_{TBF} phase while the SmC_P^H texture is cooled from a SmA_F phase.

The formation of the SmC_P^H phase clearly differs depending on the phase preceding it and here we speculate on the origin of the difference in textures. There could be a significantly larger change in pitch at the N_{TBF} - SmC_F transition vs the SmA_F - SmC_P^H , though this feels unlikely due to our expectation that the temperature dependence of the pitch at the SmA_F - SmC_P^H transition will at least be somewhat similar to that at the N_F - N_{TBF} transition i.e. a steep temperature dependence [34]. We do note a very slight unwinding of the helix just before the N_{TBF} - SmC_F transition (**fig. S13**). This is different from the much more significant unwinding of the helix observed for the transition from an N_{TBF} phase to a non-helical

SmC_P phase [35] where the helix unwinds critically.

An alternative is that forming layers in a system with an existing helical structure could result in significant defect formation due to potential deformation of the helix to form the regularly spaced smectic layers, although this does not seem to occur for the apolar twist bend nematic and associated smectic phases [42–44], though the much smaller pitch, lack of polarity and vastly different origins (electric vs elastic) make this a less than optimal comparison.

Another alternative is that the mechanism of phase structure formation in the SmC_P^H could vary significantly depending on the phase preceding it. This will mostly likely be true to some extent as observation of the temperature dependent tilt implies that the transition to the SmC_P^H phase from the SmA_F is only 2nd order while the N_{TBF} - SmC_F transition is weakly first order, however whether this explains the differences in textures vs some alternative pitch defect effect remains to be determined. It could also be reminiscent to the formation of chevron defects in the SmC^* phase where cooling from a SmA forms chevron structures due to surface pinning [45] which can be somewhat reduced when formed from a De Vries SmA phase where the randomly orientated molecular tilt reduces chevron formation [46].

V. ELECTRO-OPTICS AND FERRIELECTRIC SWITCHING

A. Current Response Measurements

The current response of the SmC_P^H of **1** in a 4 μm cell with out of plane bare ITO electrodes is not a single peak indicating complete reversal of the polarisation. Instead the current response shows a small peak pre-polarity reversal and a larger peak post-polarity reversal (**fig. 2a**). As such in the original publication [29] the phase was given the subscript designation of “**P**” to indicate polar, as the exact nature of the polarity was unclear from those

initial measurements. We suggested that the small peak is associated with the emergence of molecular tilt. From the ground state at $E = 0 \text{ V}/\mu\text{m}$ increasing the electric field results in the first large peak corresponding to the full reversal of the polarisation vector from a SmC_P^H state to a non-tilted, non-helical SmA_F state. The small peak is then the reformation of the tilt and helix. The peak cannot be due to variation in the helical pitch length as this would not modulate the polarisation beyond a small variation due to changes in the region of partial pitch that may form due to the degenerate anchoring condition of the bare ITO electrode. Variation in the tilt angle, however, would modulate the effective polarisation observed upon switching. Throughout this next section we shall refer to the smaller peak as the “tilt” peak and the larger one as the “polarisation reversal” peak.

The following discussion is given in context of the current response corresponding to a negative to positive application of electric field. Perhaps unsurprisingly the SmC_P^H phase of **2** shows a similar current response to that of **1** in terms of a tilt peak and a polarisation reversal peak (fig. 2b), although the response’s do differ in several ways. For **1** the tilt peak initially occurs at a more negative electric field ($0.43 \text{ V}/\mu\text{m}$) than for **2** ($0.1 \text{ V}/\mu\text{m}$) and is distinctly separate from the polarisation reversal peak. For **2** the peak appears the grow out of the main reversal peak seen for the N_{TBF} phase as it moves to increasingly negative voltages. We interpret this as a consequence of their different phase transitions. Presumably for **1** in the SmC_P^H phase the viscosity is similar to other smectic phases even close to the SmA_F - SmC_P^H transition while for **2** the viscosity close to the N_{TBF} - SmC_P^H transition is lower having just transitioned from the lower viscosity nematic phase. For both samples the peaks develop very similarly. Both the tilt peak and the polarisation reversal peak broaden and move to longer timescales, though this timescale shift is much more apparent for the polarisation reversal peak which may indicate that the tilt peak is less affected by the viscous-dynamics of the phase.

The electro-optic response was measured simultaneously to the current response by measuring the transmission of 589 nm light through the sample set between crossed polarisers (fig. 2). Again, as for the current response, there are similarities and differences. Both samples show changes in the transmission that couple to the tilt peak or the polarisation reversal peak prohibiting either peak being predominately due to ion flow and accumulation. The electro-optic response is horn like for both samples although clearly much sharper for **2** indicative of the lower field thresholds for the optical changes resulting in a narrowed peak. The horn shape itself can be understood by considering that transmission through a birefringent LC slab is given by:

$$\frac{T}{T_0} = \sin^2 2\phi \sin^2 \left(\frac{\pi \Delta n d}{\lambda} \right) \quad (1)$$

where T/T_0 is the transmission ratio, ϕ is the angle be-

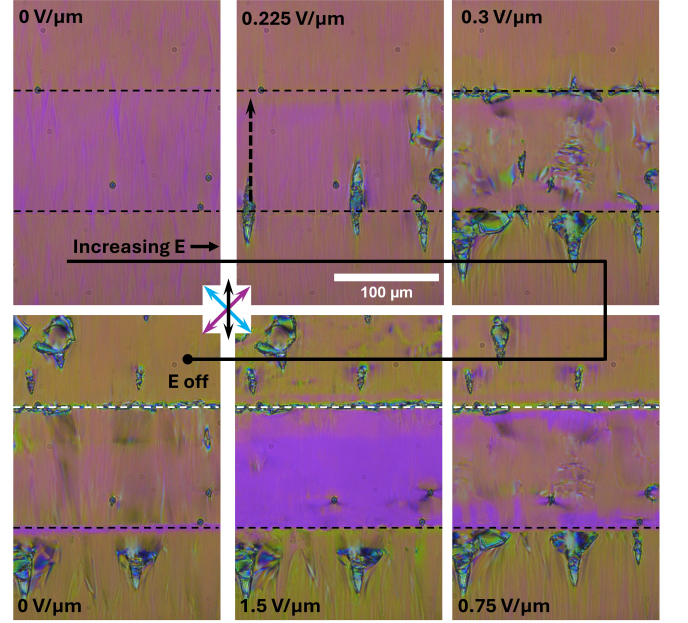


FIG. 3. POM images of compound **1** at 75 °C in the SmC_P^H phase in an IPS cell under applied field. The horizontal dashed lines indicate the limits of the active area while the vertical dashed arrow indicates the electric field direction. The cell is 5.5 μm thick with parallel rubbed planar alignment. The gap between the two electrodes is 100 μm and the DC field is initially applied anti-parallel the the initial polarisation state. For all POM images polarisor axis’ and rubbing direction are marked by the blue, purple and black arrows respectively.

tween director and polarisor, Δn is the birefringence, d the cell thickness and λ the wavelength of light. In the SmA_F state at high electric field, the transmission is a minimum as the sample has homeotropic alignment and the effective birefringence of the sample is close to zero. Reducing the electric field leads to reformation the tilt and regaining of the SmC_P^H state. The out of plane field means the homeotropic alignment is retained, and so the effective birefringence is low, leading to high transmission. As the field moves towards $0 \text{ V}/\mu\text{m}$ the homeotropic alignment is lost resulting in an increased birefringence and a loss in transmission. Increasing the field beyond the polarisation reversal peak results in a flip of the molecules and a field induced phase transition into the SmA_F state, reducing the birefringence to zero. It does not seem that the polarisation reversal motion from a SmC_P^H state to SmA_F state involves an intermediate SmC_P^H state with reversed polarisation.

For the N_{TBF} phase the current response does not show a tilt peak and only shows a single polarisation reversal peak (fig. 2c). However, it has been shown that the tilt in the N_{TBF} phase can be manipulated [34] making the lack of an obvious tilt peak surprising. This will be revisited in section V D. The electro-optic response is also strange with no significant change in transmission as a

function of the applied triangle wave. We expect that at high electric field the molecules are in the homeotropic state giving low transmission where only very small fields are required to maintain this state. At low fields the tilt is regained along with the helix resulting in reduced transmission which counteracts the increased transmission due to increased birefringence and loss of the homeotropic state.

B. In-Plane Electro-optics of the SmC_P^H Phase

To confirm that the tilt peak is indeed associated with the reformation of molecular tilt POM observation and birefringence measurements of the in-plane switching mechanism is used. Due to the strong formation of defects in the SmC_P^H of **2** (discussed in section III) we instead will mostly focus on the SmC_P^H of **1**. **1** was filled into parallel rubbed $5.5\ \mu\text{m}$ thick cell with two in-plane electrodes with a gap of $100\ \mu\text{m}$. The rubbing direction was parallel to the direction of the electric field across the electrode gap.

Applying a weak electric field ($0.225\ \text{V}/\mu\text{m}$) opposite to the initial director orientation results in the formation of elongated diamond shaped domains of reversed director (**fig. 3**). These domains grow perpendicular to the applied field until the entire active area is filled ($0.3\ \text{V}/\mu\text{m}$). They can extend beyond the active area similar to the N_F phase and in direct contrast to that of the SmA_F phase where polarisation reversal is confined to the active area [26] (**fig. 3**). This phenomena is likely due to the reduced field threshold for polarisation reversal of the SmC_P^H phase vs the SmA_F phase presumably allowing the resulting depolarisation field to propagate beyond the active area. We note that the diamond domains of reversed polarisation that form outside the active area tend to form on the side opposite to the direction of the applied field, though this does not mean that cannot form in the region in the direction of applied field. Increasing the field beyond the switching threshold sees a continuous gain in birefringence and a removal of the striations discussed in III (**fig. 3**). The final texture is uniform in colour with a birefringence value similar to that of the SmA_F phase at the SmA_F - SmC_P^H transition. Flickering undulations in the texture can be observed indicating some hydrodynamic flow due to the applied field but these do not have any obvious pattern to them. The edges of the active area show slightly different birefringence colours due to the non-uniformity of the field in those areas. Removal of the field results in a texture that is reminiscent of the initial texture though some of the reversed polarisation domains remain outside of the active area as well as a domain line along the edges of the active area indicating the different polarisation domains.

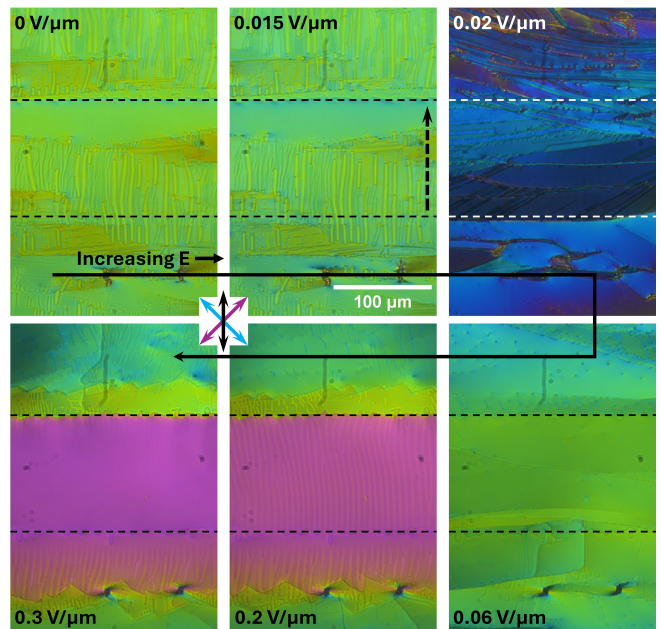


FIG. 4. POM images of compound **2** at $100\ ^\circ\text{C}$ in the N_{TBF} phase in an IPS cell under application of a DC electric field. The horizontal dashed lines indicate the limits of the active area while the vertical dashed arrow indicates the electric field direction. The cell is $5.5\ \mu\text{m}$ thick with parallel rubbed planar alignment. The gap between the two electrodes is $100\ \mu\text{m}$ and the DC field is initially applied anti-parallel the the initial polarisation state. For all POM images polarisor axis' and rubbing direction are marked by the blue, purple and black arrows respectively.

C. In-Plane Electro-optics of the N_{TBF} Phase

The current response of the SmC_P^H phase clearly shows a second peak which we have shown to be related to tilt reformation indicating that the larger polarisation reversal peak also contains a field induced phase transition back into the SmA_F phase. The N_{TBF} phase is also heliconical but its current response does not show a second peak to associate with any field induced transition. To investigate whether full tilt removal is still possible we probe the N_{TBF} phase via in-plane switching observations in the same $5.5\ \mu\text{m}$ thick parallel rubbed cells as for the SmC_P^H phase.

The transition to the from the N_F phase to N_{TBF} phase is clear by the formation of stripes parallel to the rubbing direction (**fig. 4**). As the temperature is decreased these stripes split along the rubbing direction into regions of stripe domains and uniform texture. Since these stripes are parallel to the rubbing direction and thus parallel to the helicoidal axis, they are not pitch repeat units. These are not regions of opposite polarity as they remain under application of a moderate in-plane dc field and a strong field removes them without evidence of polarisation reversal.

For the N_{TBF} phase the direction of the in-plane polar-

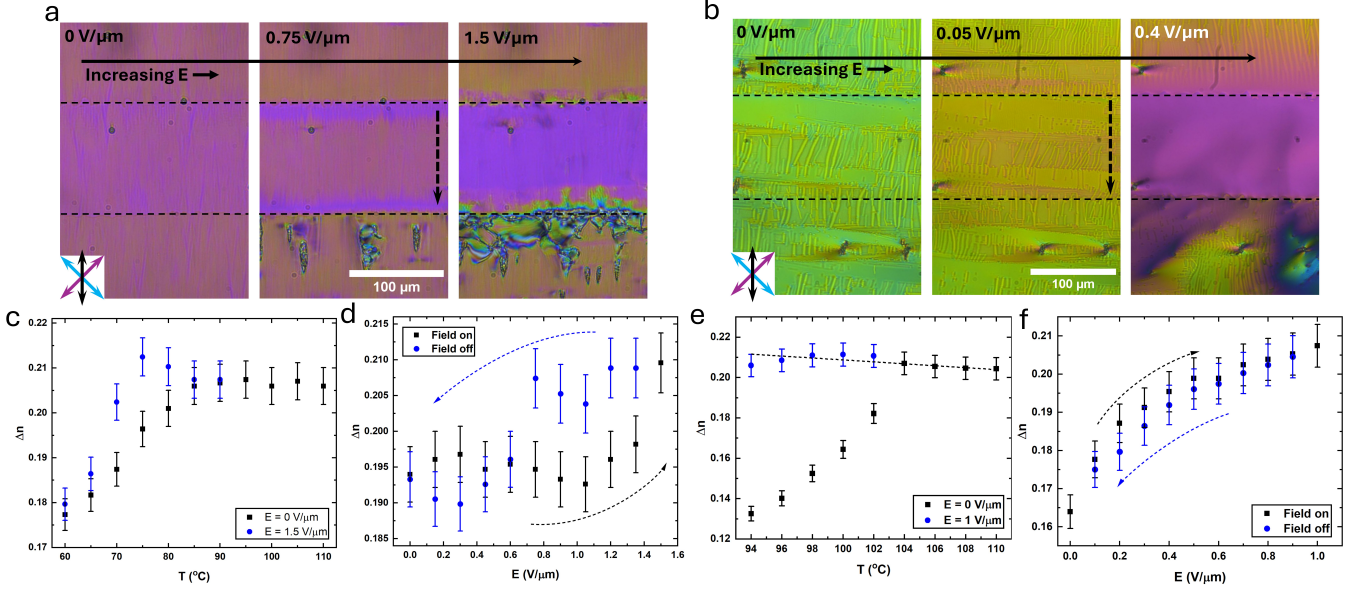


FIG. 5. POM images of **a)** compound **1** at 75 °C in the SmC_P^H phase and **b)** compound **2** at 100 °C in the N_{TBF} phase both an IPS cell under application of a DC electric field where the cell is 5.5 μm thick with parallel rubbed planar alignment. Here the DC field is applied syn-parallel to the polarisation direction. For all POM images polarisor axis' and rubbing direction are marked by the blue, purple and black arrows respectively. Temperature dependence of the birefringence of **c)** **1** and **e)** **2** both with and without an applied DC field. Electric field dependence of the birefringence of **d)** compound **1** at 75 °C and **f)** compound **2** at 100 °C indicating the hysteresis of the tilt removal for the SmC_P^H phase and the lack of hysteresis for the N_{TBF} phase.

ity can be switched by a dc in-plane electric field just as for the N_F [17, 25, 47, 48] although the switching is somewhat different. At low dc fields (below $\sim 0.02 \text{ V}/\mu\text{m}$) there is a small reduction in birefringence without significant disruption of the texture (**fig. 4**), consistent with the N_F phase where this behaviour has been associated with increased director twist [48]. At a critical voltage ($\sim 0.02 \text{ V}/\mu\text{m}$) there is a significant reduction in birefringence and the sample breaks into many domains (**fig. 4**). Slight uncrossing of the polarisers does not reveal any difference in optical activity of these domains. As the voltage is increased further (up to $0.06 \text{ V}/\mu\text{m}$) these domains coalesce and there is a steady increase in birefringence up to the amount of the unperturbed N_{TBF} state with no signs of the undulations found in that unperturbed state (**fig. 4**). Further increase in the voltage sees an increase in the birefringence beyond the unperturbed state and eventually (above $0.15 \text{ V}/\mu\text{m}$) the undulations return before finally (around $0.3 \text{ V}/\mu\text{m}$) obtaining a uniform N_F like texture with a birefringence similar to that of the N_F phase just before transition to the N_{TBF} phase. Just as for the SmC_P^H phase the effect of the in-plane field can extend beyond the active area. However, due to the lower threshold for switching in the N_{TBF} phase, the full polarisation reversal spreads significantly beyond the active area and it is just the increase of birefringence that is limited to the out of active area region opposite the applied field. It is clear that both the SmC_P^H and N_{TBF} phases can undergo a field induced phase transition the

untitled state which by necessity would remove the helix entirely.

D. Ferrielectric Switching in the SmC_P^H Phase

Applying a electric field anti-parallel to the polarisation axis of both the SmC_P^H and N_{TBF} phases results in full reversal of the polarisation direction. Further increase in the field results in an increase in birefringence where this second stage is due to the reduction in molecular tilt. If the electric field is applied syn-parallel to the polarisation direction no reversal in the polarisation direction is observed. However, an increase in birefringence, associated with the tilt removal, is still observed for both phases (**fig. 4**). If the field is removed the tilt is reformed and a drop in birefringence back to the original value is observed. For the SmC_P^H phase of **1**, full tilt removal could only be completed in a specific temperature window close to the $\text{SmA}_F - \text{SmC}_P^H$ transition (**fig. 5a**) due to an increase in field threshold for this effect. Presumably if higher electric fields were achieved, either through higher voltages or a narrower active area, full tilt removal could be completed for the entire phase window. For the N_{TBF} phase of **2** full tilt removal could be completed for the entire phase (**fig. 5b**). We also note that if an in-plane field is applied to the SmC_P^H phase of **2** a uniform birefringent texture could be obtained (**fig. S3**) which reverted back to the defect texture upon removal of

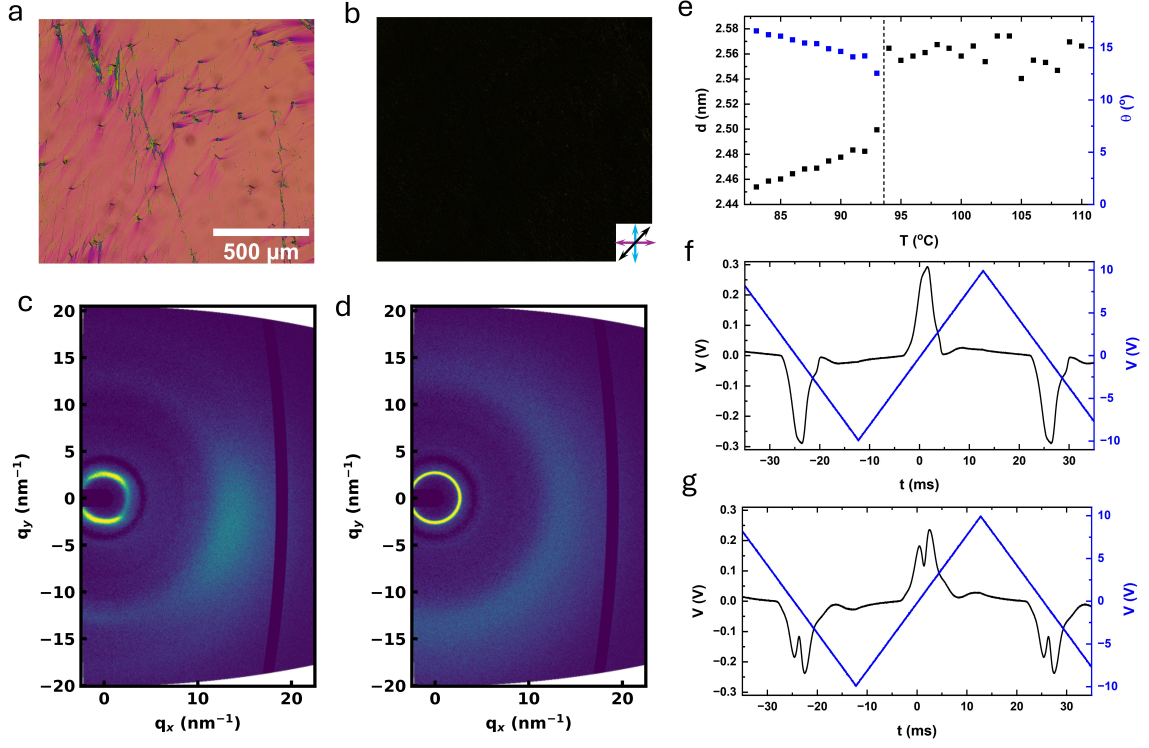


FIG. 6. POM images in the a) N_F and b) SmC_P^H phases of **3** in a 5 μm planar aligned parallel rubbed cell. Arrows indicate direction of polarisers and rubbing direction. 2D X-ray scattering images of **3** in the c) N_F and d) SmC_P^H phases. e) Temperature dependence of the d-spacing and molecular tilt of **3**. Current responses for **3** in the f) N_F and g) SmC_P^H phases.

the field indicating that tilt removal is possible here too. The hysteresis of tilt removal and switching behaviour is clear also in out of plane measurements (fig. S4) where tilt is clearly recovered only at lower field strength values than it is lost.

To investigate the threshold and field dependence of the tilt removal we measure birefringence as a function of applied field. This is measured in the very centre of the active area where the in-plane field is most parallel to the cell plane. For the SmC_P^H phase of **1** we see that the birefringence only increases after some critical value where it sharply increases up to a value slightly beyond that of the untitled SmA_F phase. We attribute this increase beyond the SmA_F value either due to a increase in alignment quality over that of the SmA_F or some electrically modified order parameter effect [49]. When the field is reduced the increased birefringence is retained to lower voltages than the threshold for tilt removal indicating a hysteresis in the tilt removal (fig. 5c). For analogous measurements on the N_{TBF} phase of **2** the tilt removal is threshold-less, despite the presence of an alignment layer, and has no evidence of hysteresis (fig. 5d). The threshold-less nature of the change in tilt is due to the avoidance of bound charges that would form in the bulk. Instead, the tilt is maintained homogenous across the active area and bound charges are expelled to the electrodes, similar to director oscillations in the N_F

phase [50]. The obtained birefringence is slightly higher than the N_F phase however not as significant as for the SmC_P^H phase.

The helix in the the SmC_P^H and N_{TBF} phases allows for partial polarisation compensation and so removal of the tilt results in an increase in polarisation. A ferroelectric phase has two stable states at $E = 0$ while an anti-ferroelectric phase would only have a single stable state [51]. A ferrielectric phase has two stable states at $E = 0$ but two separate sub-lattices of non-equal polarisation [52]. These sub-lattices can be reversed going through a field-induced phase transition to the ferroelectric state at high electric field. As a result a ferrielectric phase has three hysteresis loops in its P-E curve

The SmC_P^H phase has three separate hysteresis components (polarisation reversal and then tilt hysteresis in both the positive and negative polarisation states) and so has a pseudo-ferrielectric switching response. However, it is not a true ferrielectric phase as its ground state is ferroelectric like with all of its constituent dipoles orientated along the same direction. The N_{TBF} phase has the same ground state as the SmC_P^H but does not exhibit hysteresis in its tilt removal and so only exhibits ferroelectric switching with an additional pseudo-paraelectric component at higher electric fields.

Beyond the N_{TBF} phase, current responses consisting of a small peak pre-polarity reversal and a sub-

sequent larger peak have been observed for the non-helical SmC_P phase [30, 32, 53], though this is apparently not always observed [31]. This peak has been associated with tilt reformation and indicates the possibility of a pseudo-ferrielectric responses for the the non-helical SmC_P phase.

VI. PRE-TRANSITIONAL HELIX FORMATION

We have demonstrated how variation of the phase ordering from $\text{SmC}_P^H\text{-N}_{\text{TBF}}\text{-N}_F$ to $\text{SmC}_P^H\text{-SmA}_F$ varies the properties of the SmC_P^H phase. Both of the aforementioned transitions to heliconic order are 2nd order indicated by their lack of enthalpy from DSC and their continuous, rather than discontinuous, tilt dependence at the transition to heliconic order (fig. S11). Variation in fluorination is a now well established technique to obtain various polar phases [24, 35, 54] and so changing the chemical structure to that of compound **3** (tbl. I) results in a phase order of $\text{N}_F\text{-SmC}_P^H$. POM observations reveal the $\text{SmC}_P^H\text{-N}_F$ transition on cooling occurs as a wave edged with dendritic tendrils (fig. 6a,b). The transition front moves across the cell, forming a similar scattering texture as observed for **2**, nucleating from specific points across the cell. This is contrary to the smooth uniform change in texture as observed for the $\text{N}_{\text{TBF}}\text{-N}_F$ transition of **2**. On heating the scattering texture melts with a sharp boundary between SmC_P^H and N_F domains.

X-ray scattering measurements show a large jump in tilt angle formation up to $\sim 12^\circ$ molecular tilt immediately at the transition indicating a strong first order character (fig. 6c-e). We also observe a comparatively large enthalpy compared to the lack of enthalpy for the 2nd order transitions $\text{SmC}_P^H\text{-SmA}_F$ and $\text{N}_{\text{TBF}}\text{-N}_F$ as well as the 1st order $\text{SmC}_P^H\text{-N}_{\text{TBF}}$ transition. All of this points to the $\text{SmC}_P^H\text{-N}_F$ transition of **3** as being the first 1st order transition to spontaneous heliconic order. Current response measurements show a single polarisation reversal peak for the N_F phase (fig. 6f). Upon transition into the SmC_P^H phase the peak splits into two with a smaller tilt peak at pre-polarity voltages and larger polarisation reversal peak (fig. 6g) which moves to longer time scales with reducing temperature. The larger initial size of the tilt peak is owed to the first order nature of the transition leading to an discontinuous large change in the molecular tilt and so a larger change in polarisation upon tilt reformation.

If the boundary between the N_F and SmC_P^H domains is observed on cooling, a narrow region of $\sim 300\ \mu\text{m}$ width exists where selective reflection can be seen (fig. 7a). Across this boundary layer the colour varies from red to purple indicating an increasing in bandgap wavelength from the SmC_P^H domain to the N_F domain. Measuring the wavelength of the selective reflection directly shows it does indeed shift rapidly though the visible window in 0.2°C indicating rapid change of the helical pitch in this region (fig. 7c). Direct remeasurements of the pitch

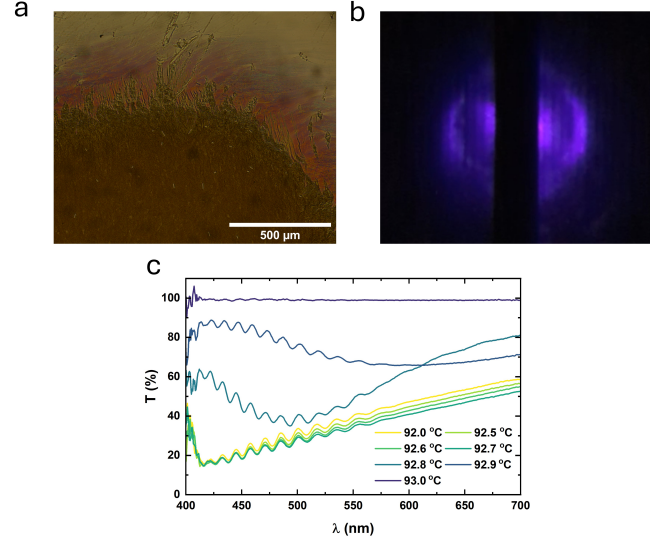


FIG. 7. **a)** Microscopy image with the polarisor inserted parallel to the rubbing direction (no analyser) of the boundary between the N_F phase (top) and SmC_P^H phase (bottom) showing selective reflection in the boundary region. **b)** diffraction pattern from the boundary region demonstrating a pitch of $\sim 800\ \mu\text{m}$. **c)** Transmission spectrum from the boundary region of image **a)**.

via laser diffraction confirm this indicating a change in pitch from $920\ \mu\text{m}$ to less than $600\ \mu\text{m}$ within that same 0.2°C window (fig. 7b). We considered whether this is a narrow temperature window of N_{TBF} phase existence, however on heating the region of selective reflection and light diffraction due to the helical pitch is not observed (videos 1 and 2). We interpret this as either the SmC_P^H phase front growing across the cell and forming initially in a thin area nearer the base due to any vertical temperature gradients which then produces the selective reflection and pitch. Alternatively this is a pre-transitional effect where the helix in the SmC_P^H acts in induce some helical ordering in the neighbouring N_F regions. As this is not the lowest free energy state for the N_F phase this helix unwinds as distance from the phase front is increased until it smoothly merges with the non-helical N_F regions.

VII. CONCLUSION

The discovery of spontaneous chiral symmetry breaking in the ferroelectric nematic realm [29, 34] is extremely exciting due to the potential for replicating the behaviours seen in hard matter systems such as ferromagnets in fluid soft matter systems. Here we have demonstrated that the SmC_F phase found in **2** [34] is helical and is in fact a SmC_P^H phase, as observed for **1** [29]. We show that there is at least three phase pathways to the SmC_P^H (we expect that there could well be more pathways than the three presented here). Namely $\text{SmC}_P^H\text{-SmA}_F$, $\text{SmC}_P^H\text{-N}_{\text{TBF}}$

N_{TBF} and $\text{SmC}_P^{\text{H}}\text{-N}_F$ and that each leads to an array of different polymorphs and interesting properties.

We account for the double peak structure of the current response for the SmC_P^{H} phase, demonstrating that the smaller pre-polarity peak is associated with reformation of the tilt and show how the behaviour of this tilt peak is influenced by the phase preceding it. The tilt peak of the SmC_P^{H} phase is indicative of field induced phase transitions to the SmA_F state. This phase transition shows clear hysteresis indicating that it is pseudo-ferrielectric due to the increase in polarisation that occurs by removing molecular tilt from a partially compensated helical phase.

Looking forward, spontaneous symmetry breaking due to polar order may yield interesting new phase types when superimposed on more complex liquid crystal organisations, for example the twist grain boundary like polar twisted smectic structures described recently by Nishikawa et. al. [55]

DATA AVAILABILITY

The data associated with this paper are openly available from the University of Leeds Data Repository at: <https://doi.org/10.5518/1643>

AUTHOR CONTRIBUTION STATEMENT

JH and CJG contributed equally to this work. The manuscript was written, reviewed, and edited with contributions from all authors.

COMPETING INTERESTS

Authors declare that they have no competing interests

ACKNOWLEDGEMENTS

RJM thanks UKRI for funding via a Future Leaders Fellowship, grant number MR/W006391/1, and the University of Leeds for funding via a University Academic Fellowship. The SAXS/WAXS system used in this work was funded by EPSRC via grant number EP/X0348011. R.J.M. gratefully acknowledge support from Merck KGaA. Computational work was performed on ARC3 and ARC4, part of the high-performance computing facilities at the University of Leeds.

-
- [1] D. G. Blackmond, The origin of biological homochirality, *Cold Spring Harbor Perspectives in Biology* **2**, a002147 (2010).
 - [2] Z. Shen, Y. Sang, T. Wang, J. Jiang, Y. Meng, Y. Jiang, K. Okuro, T. Aida, and M. Liu, Asymmetric catalysis mediated by a mirror symmetry-broken helical nanoribbon, *Nature Communications* **10**, 3976 (2019).
 - [3] P. W. Higgs, Broken symmetries and the masses of gauge bosons, *Phys. Rev. Lett.* **13**, 508 (1964).
 - [4] F. Gu, B. Guiselin, N. Bain, I. Zuriguel, and D. Bartolo, Emergence of collective oscillations in massive human crowds, *Nature* **638**, 112 (2025).
 - [5] C. Tschierske, Mirror symmetry breaking in liquids and liquid crystals, *Liquid Crystals* **45**, 2221 (2018).
 - [6] S. T. Lagerwall, Ferroelectric and antiferroelectric liquid crystals, *Ferroelectrics* **301**, 15 (2004).
 - [7] H. Takezoe, E. Gorecka, and M. Čepič, Antiferroelectric liquid crystals: Interplay of simplicity and complexity, *Rev. Mod. Phys.* **82**, 897 (2010).
 - [8] A. Eremin and A. Jákli, Polar bent-shape liquid crystals – from molecular bend to layer splay and chirality, *Soft Matter* **9**, 615 (2013).
 - [9] A. Jákli, O. D. Lavrentovich, and J. V. Selinger, Physics of liquid crystals of bent-shaped molecules, *Rev. Mod. Phys.* **90**, 045004 (2018).
 - [10] S. P. Sreenilayam, Y. P. Panarin, J. K. Vij, V. P. Panov, A. Lehmann, M. Poppe, M. Prehm, and C. Tschierske, Spontaneous helix formation in non-chiral bent-core liquid crystals with fast linear electro-optic effect, *Nature Communications* **7**, 11369 (2016).
 - [11] C. T. Imrie, R. Walker, J. M. D. Storey, E. Gorecka, and D. Pociecha, Liquid crystal dimers and smectic phases from the intercalated to the twist-bend, *Crystals* **12**, 1245 (2022).
 - [12] R. J. Mandle, A ten-year perspective on twist-bend nematic materials, *Molecules* **27**, 2689 (2022).
 - [13] R. J. Mandle, S. J. Cowling, and J. W. Goodby, A nematic to nematic transformation exhibited by a rod-like liquid crystal, *Phys. Chem. Chem. Phys.* **19**, 11429 (2017).
 - [14] R. J. Mandle, S. J. Cowling, and J. W. Goodby, Rational design of rod-like liquid crystals exhibiting two nematic phases, *Chemistry – A European Journal* **23**, 14554 (2017).
 - [15] H. Nishikawa, K. Shiroshita, H. Higuchi, Y. Okumura, Y. Haseba, S.-i. Yamamoto, K. Sago, and H. Kikuchi, A fluid liquid-crystal material with highly polar order, *Advanced Materials* **29**, 1702354 (2017).
 - [16] A. Mertelj, L. Cmok, N. Sebastián, R. J. Mandle, R. R. Parker, A. C. Whitwood, J. W. Goodby, and M. Čopič, Splay nematic phase, *Phys. Rev. X* **8**, 041025 (2018).
 - [17] X. Chen, E. Korblva, D. Dong, X. Wei, R. Shao, L. Radzihovsky, M. A. Glaser, J. E. MacLennan, D. Bedrov, D. M. Walba, and N. A. Clark, First-principles experimental demonstration of ferroelectricity in a thermotropic nematic liquid crystal: Polar domains and striking electro-optics, *Proceedings of the National Academy of Sciences* **117**, 14021 (2020).
 - [18] N. Sebastián, L. Cmok, R. J. Mandle, M. R. de la Fuente, I. Drevenšek Olenik, M. Čopič, and A. Mertelj, Ferroelectric-ferroelastic phase transition in a nematic

- liquid crystal, *Phys. Rev. Lett.* **124**, 037801 (2020).
- [19] R. J. Mandle, N. Sebastián, J. Martínez-Perdiguero, and A. Mertelj, On the molecular origins of the ferroelectric splay nematic phase, *Nature Communications* **12**, 4962 (2021).
 - [20] J. Li, H. Nishikawa, J. Kougo, J. Zhou, S. Dai, W. Tang, X. Zhao, Y. Hisai, M. Huang, and S. Aya, Development of ferroelectric nematic fluids with giant- ϵ dielectricity and nonlinear optical properties, *Science Advances* **7**, eabf5047 (2021).
 - [21] N. Sebastián, M. Čopič, and A. Mertelj, Ferroelectric nematic liquid-crystalline phases, *Phys. Rev. E* **106**, 021001 (2022).
 - [22] P. Kumari, B. Basnet, M. O. Lavrentovich, and O. D. Lavrentovich, Chiral ground states of ferroelectric liquid crystals, *Science* **383**, 1364 (2024).
 - [23] E. Cruickshank, The emergence of a polar nematic phase: A chemist's insight into the ferroelectric nematic phase, *ChemPlusChem* **89**, e202300726 (2024).
 - [24] C. J. Gibb, J. Hobbs, and R. J. Mandle, Systematic fluorination is a powerful design strategy toward fluid molecular ferroelectrics, *Journal of the American Chemical Society* **147**, 4571 (2025).
 - [25] X. Chen, E. Korblova, M. A. Glaser, J. E. MacLennan, D. M. Walba, and N. A. Clark, Polar in-plane surface orientation of a ferroelectric nematic liquid crystal: Polar monodomains and twisted state electro-optics, *Proceedings of the National Academy of Sciences* **118**, e2104092118 (2021).
 - [26] X. Chen, V. Martinez, P. Nacke, E. Korblova, A. Manabe, M. Klasen-Memmer, G. Freychet, M. Zhernenkov, M. A. Glaser, L. Radzihovsky, J. E. MacLennan, D. M. Walba, M. Bremer, F. Giesselmann, and N. A. Clark, Observation of a uniaxial ferroelectric smectic a phase, *Proceedings of the National Academy of Sciences* **119**, e2210062119 (2022).
 - [27] H. Kikuchi, H. Matsukizono, K. Iwamatsu, S. Endo, S. Anan, and Y. Okumura, Fluid layered ferroelectrics with global $C_{\infty v}$ symmetry, *Advanced Science* **9**, 2202048 (2022).
 - [28] X. Chen, V. Martinez, E. Korblova, G. Freychet, M. Zhernenkov, M. A. Glaser, C. Wang, C. Zhu, L. Radzihovsky, J. E. MacLennan, D. M. Walba, and N. A. Clark, The smectic z_A phase: Antiferroelectric smectic order as a prelude to the ferroelectric nematic, *Proceedings of the National Academy of Sciences* **120**, e2217150120 (2023).
 - [29] C. J. Gibb, J. Hobbs, D. I. Nikolova, T. Raistrick, S. R. Berrow, A. Mertelj, N. Osterman, N. Sebastián, H. F. Gleeson, and R. J. Mandle, Spontaneous symmetry breaking in polar fluids, *Nature Communications* **15**, 5845 (2024).
 - [30] J. Hobbs, C. J. Gibb, D. Pociecha, J. Szydłowska, E. Górecka, and R. J. Mandle, Polar order in a fluid like ferroelectric with a tilted lamellar structure – observation of a polar smectic c (SmC_P) phase, *Angewandte Chemie International Edition* **64**, e202416545 (2025).
 - [31] H. Kikuchi, H. Nishikawa, H. Matsukizono, S. Iino, T. Sugiyama, T. Ishioka, and Y. Okumura, Ferroelectric smectic c liquid crystal phase with spontaneous polarization in the direction of the director, *Advanced Science* **11**, 2409827 (2024).
 - [32] G. J. Strachan, E. Górecka, J. Szydłowska, A. Makal, and D. Pociecha, Nematic and smectic phases with proper ferroelectric order, *Advanced Science* , 2409754 (2024).
 - [33] P. Medle Rupnik, E. Hanžel, M. Lovšin, N. Osterman, C. J. Gibb, R. J. Mandle, N. Sebastián, and A. Mertelj, Antiferroelectric order in nematic liquids: Flexoelectricity versus electrostatics, *Advanced Science* , 2414818 (2025).
 - [34] J. Karcz, J. Herman, N. Rychłowicz, P. Kula, E. Górecka, J. Szydłowska, P. W. Majewski, and D. Pociecha, Spontaneous chiral symmetry breaking in polar fluid–heliconal ferroelectric nematic phase, *Science* **384**, 1096 (2024).
 - [35] G. J. Strachan, E. Górecka, J. Hobbs, and D. Pociecha, Fluorination: Simple change but complex impact on ferroelectric nematic and smectic liquid crystal phases, *Journal of the American Chemical Society* 10.1021/jacs.4c16802 (2025).
 - [36] H. Nishikawa, D. Okada, D. Kwaria, A. Nihonyanagi, M. Kuwayama, M. Hoshino, and F. Araoka, Emergent ferroelectric nematic and heliconal ferroelectric nematic states in an achiral “straight” polar rod mesogen, *Advanced Science* **11**, 2405718 (2024).
 - [37] J. Hobbs, C. J. Gibb, and R. J. Mandle, Emergent antiferroelectric ordering and the coupling of liquid crystalline and polar order, *Small Science* **4**, 2400189 (2024).
 - [38] K. G. Hedlund, V. Martinez, X. Chen, C. S. Park, J. E. MacLennan, M. A. Glaser, and N. A. Clark, Freely suspended nematic and smectic films and free-standing smectic filaments in the ferroelectric nematic realm, *Phys. Chem. Chem. Phys.* 10.1039/D4CP03425B (2025).
 - [39] N. A. Clark and P. S. Pershan, Light scattering by deformation of the plane texture of smectic and cholesteric liquid crystals, *Phys. Rev. Lett.* **30**, 3 (1973).
 - [40] D. Demus, S. Diele, S. Grande, and H. Sackmann, Polymorphism in thermotropic liquid crystals, in *Advances in Liquid Crystals*, Vol. 6, edited by G. H. Brown (Elsevier, 1983).
 - [41] X. Chen, Z. Zhu, M. J. Magrini, E. Korblova, C. S. Park, M. A. Glaser, J. E. MacLennan, D. M. Walba, and N. A. Clark, Ideal mixing of paraelectric and ferroelectric nematic phases in liquid crystals of distinct molecular species, *Liquid Crystals* **49**, 1531 (2022).
 - [42] R. Walker, D. Pociecha, G. J. Strachan, J. M. D. Storey, E. Gorecka, and C. T. Imrie, Molecular curvature, specific intermolecular interactions and the twist-bend nematic phase: the synthesis and characterisation of the 1-(4-cyanobiphenyl-4'-yl)-6-(4-alkylanilinebenzylidene-4'-oxy)hexanes (CB6O.m), *Soft Matter* **15**, 3188 (2019).
 - [43] D. Pociecha, N. Vaupotič, M. Majewska, E. Cruickshank, R. Walker, J. M. D. Storey, C. T. Imrie, C. Wang, and E. Gorecka, Photonic bandgap in achiral liquid crystals—a twist on a twist, *Advanced Materials* **33**, 2103288 (2021).
 - [44] A. F. Alshammari, A. Zattarin, A. Pearson, E. Cruickshank, M. Majewska, D. Pociecha, J. M. Storey, E. Gorecka, C. T. Imrie, and R. Walker, Heliconal nematic and smectic phases: the synthesis and characterisation of the CB4O.m and CB8O.m series, *Liquid Crystals* , 1 (2024).
 - [45] T. P. Rieker, N. A. Clark, G. S. Smith, D. S. Parmar, E. B. Sirota, and C. R. Safinya, "chevron" local layer structure in surface-stabilized ferroelectric smectic-c cells, *Phys. Rev. Lett.* **59**, 2658 (1987).
 - [46] J. P. F. Lagerwall and F. Giesselmann, Current topics in smectic liquid crystal research, *ChemPhysChem* **7**, 20 (2006).

- [47] N. Sebastián, R. J. Mandle, A. Petelin, A. Eremin, and A. Mertelj, Electrooptics of mm-scale polar domains in the ferroelectric nematic phase, *Liquid Crystals* **48**, 2055 (2021).
- [48] B. Basnet, M. Rajabi, H. Wang, P. Kumari, K. Thapa, S. Paul, M. O. Lavrentovich, and O. D. Lavrentovich, Soliton walls paired by polar surface interactions in a ferroelectric nematic liquid crystal, *Nature Communications* **13**, 3932 (2022).
- [49] K. Thapa, S. Paladugu, and O. D. Lavrentovich, Microsecond electro-optic switching in the nematic phase of a ferroelectric nematic liquid crystal, *Opt. Express* **32**, 40274 (2024).
- [50] B. Basnet, S. Paladugu, O. Kurochkin, O. Buluy, N. Aryasova, V. G. Nazarenko, S. V. Shiyanovskii, and O. D. Lavrentovich, Periodic splay fréedericksz transitions in a ferroelectric nematic, *Nature Communications* **16**, 1444 (2025).
- [51] S. T. Lagerwall, Ferroelectric liquid crystals, in *Handbook of Liquid Crystals* (John Wiley & Sons, Ltd, 2014) Chap. 5.
- [52] Z. Fu, X. Chen, Z. Li, T. Hu, L. Zhang, P. Lu, S. Zhang, G. Wang, X. Dong, and F. Xu, Unveiling the ferroelectric nature of pbzro3-based antiferroelectric materials, *Nature Communications* **11**, 3809 (2020).
- [53] D. Węglowska, M. Czerwiński, R. Dzienisiewicz, P. Perkowski, J. Szydłowska, D. Pocięcha, and M. Mrukiewicz, The balance between paraelectricity and ferroelectricity in non-chiral smectic homologs (2024), arXiv:2412.20508 [cond-mat.mtrl-sci].
- [54] E. Cruickshank, R. Walker, G. J. Strachan, E. Górecka, D. Pocięcha, J. M. D. Storey, and C. T. Imrie, The role of fluorine substituents in the formation of the ferroelectric nematic phase, *J. Mater. Chem. C* 10.1039/D4TC03318C (2025).
- [55] H. Nishikawa, Y. Okumura, D. Kwaria, A. Nihonyanagi, and F. Araoka, Spontaneous twist of ferroelectric smectic blocks in polar fluids (2025), arXiv:2502.03319 [cond-mat.soft].

Supplementary Information:

Ferri- and Ferro-Electric Switching in Spontaneously Chiral Polar Liquid Crystals

Jordan Hobbs^{1,*}, Calum J. Gibb², and Richard. J. Mandle^{1,2}

¹*School of Physics & Astronomy, University of Leeds, UK and*

²*School of Chemistry, University of Leeds, UK*

(Dated: February 13, 2025)

CONTENTS

1. Supplementary methods
2. Supplementary results
3. Organic synthesis
4. Supplementary References

1. SUPPLEMENTARY METHODS

1.1. Chemical Synthesis

Chemicals were purchased from commercial suppliers (Fluorochem, Merck, ChemScene, Ambeed) and used as received. Solvents were purchased from Merck and used without further purification. Reactions were performed in standard laboratory glassware at ambient temperature and atmosphere and were monitored by TLC with an appropriate eluent and visualised with 254 nm light. Chromatographic purification was performed using a Combiflash NextGen 300+ System (Teledyne Isco) with a silica gel stationary phase and a hexane/ethyl acetate gradient as the mobile phase, with detection made in the 200-800 nm range. Chromatographed materials were filtered through 200 nm PTFE frits and then subjected to re-crystallisation from an appropriate solvent system.

* j.l.hobbs@leeds.ac.uk

1.2. Chemical Characterisation

Chemical materials were characterised by NMR spectroscopy using a Bruker Avance III HDNMR spectrometer operating at 400 MHz, 100.5 MHz or 376.4 MHz (^1H , ^{13}C and ^{19}F , respectively). High resolution mass spectrometry data (HRMS) was collected using a Bruker MaXis Impact spectrometer with a negative ESI source (VIP-HESI); the sample was introduced via direct infusion as solution in MeCN. HPLC analysis was performed using an Agilent 1290 Infinity II system fitted with a poroshell 120 ec-c18 column running a water:MeCN gradient.

1.3. Thermal Analysis

Differential scanning calorimetry (DSC) measurements were performed using a TA Instruments Q2000 DSC instrument (TA Instruments, Wilmslow UK), equipped with a RCS90 Refrigerated cooling system (TA Instruments, Wilmslow UK). The instrument was calibrated against an Indium standard, and data were processed using TA Instruments Universal Analysis Software. Samples were analysed under a nitrogen atmosphere, in hermetically sealed aluminium TZero crucibles (TA Instruments, Wilmslow, UK) and subjected to three analysis cycles. In all cases, samples were subject to heating and cooling at a rate of 10 K min⁻¹. Phase transition temperatures were measured as onset values on cooling cycles for consistency between monotropic and enantiotropic phase transitions, while crystal melts were obtained as onset values on heating.

1.3. Optical Microscopy

Polarised light optical microscopy (POM) was performed using a Leica DM2700P polarised light microscope (Leica Microsystems (UK) Ltd., Milton Keynes, UK), equipped with 10x and 50x magnification, and a rotatable stage. A Linkam TMS 92 heating stage (Linkam Scientific Instruments Ltd., Redhill, UK) was used for temperature control, and samples were studied sandwiched between two untreated glass coverslips. Images were recorded using a Nikon D3500 Digital Camera (Nikon UK Ltd., Surbiton, UK), using DigiCamControl software.

1.4. X-ray Scattering

X-ray scattering measurements, both small angle (SAXS) and wide angle (WAXS) were recorded using an Anton Paar SAXSpoint 5.0 beamline machine. This was equipped with a primux 100 Cu X-ray source with a 2D EIGER2 R detector. The X-rays had a wavelength of 0.154 nm. Samples were filled into either thin-walled quartz capillaries or held between Kapton tape. Temperature was controlled using an Anton Paar heated sampler with a range of -10 °C to 120°C and the samples held in a chamber with an atmospheric pressure of <1 mbar. Samples were held at 120°C to allow for temperature equilibration across the sample and then slowly cooled while stopping to record the scattering patterns.

The samples were not formally aligned and so these measurements can be considered as “powder” samples. It should be noted that some spontaneous alignment of the LCs both within the capillaries and between the Kapton tape did occur leading to the classic “lobe” pattern seen in the 2D patterns. 1D patterns were obtained by radially integrating the 2D SAXS patterns. Peak position and FWHM was recorded and then converted into d spacing following Bragg’s law. In the tilted smectic phase, the tilt was obtained from:

$$\frac{d_c}{d_A} = \cos \theta \quad (1)$$

where d_c is the layer spacing in the tilted smectic phase, d_A is the extrapolated spacing from the non-tilted preceding phase, extrapolated to account for the weak temperature dependence of the preceding phases due to shifts in conformation and order, and θ the structural tilt angle.

1.5. Measurement of Spontaneous Polarization (P_S)

Spontaneous polarisation measurements are undertaken using the current reversal technique. Triangular waveform AC voltages are applied to the sample cells with an Agilent 33220A signal generator (Keysight Technologies), and the resulting current outflow is passed through a current-to-voltage amplifier and recorded on a RIGOL DHO4204 high-resolution oscilloscope (Telonic Instruments Ltd, UK). Heating and cooling of the samples during these measurements is achieved with an Instec HCS402 hot stage controlled to 10 mK stability by an Instec mK1000 temperature controller. The LC samples are held in 4µm thick cells with no alignment layer, supplied by Instec. The measurements consist of cooling the sample at

a rate of 1 Kmin⁻¹ and applying a set voltage at a frequency of 20 Hz to the sample every 1 K. The voltage was set such that it would saturate the measured P_S and was determined before final data collection.

There are three contributions to the measured current trace: accumulation of charge in the cell (I_c), ion flow (I_i), and the current flow due to polarisation reversal (I_p). To obtain a P_S value, we extract the latter, which manifests as one or multiple peaks in the current flow, and integrate as:

$$P_S = \int \frac{I_p}{2A} dt \quad (2)$$

where A is the active electrode area of the sample cell.

1.6. Birefringence Measurements

Birefringence was measured using a Berek compensator mounted in a Leica DM 2700 P polarised optical microscope. The birefringence was measured in the centre of the active ITO area for the IPS cells used here.

1.7. Transmission Spectra

A microscope equipped coupled to an Avantes AvaSpec-2048 XL spectrometer which used to record transmission spectra of samples. The rubbing direction was set parallel to the light polarization direction, but no analyzer was inserted. A spectra from the phase above the spontaneously chiral phases was used as the reference state of each sample

1.8. Pitch Measurements

The pitch was measured by illumination of the sample from the bottom via a 405 nm laser. The angle of diffraction was measured on a flat screen set 1.8cm away from the sample.

2. SUPPLEMENTARY RESULTS

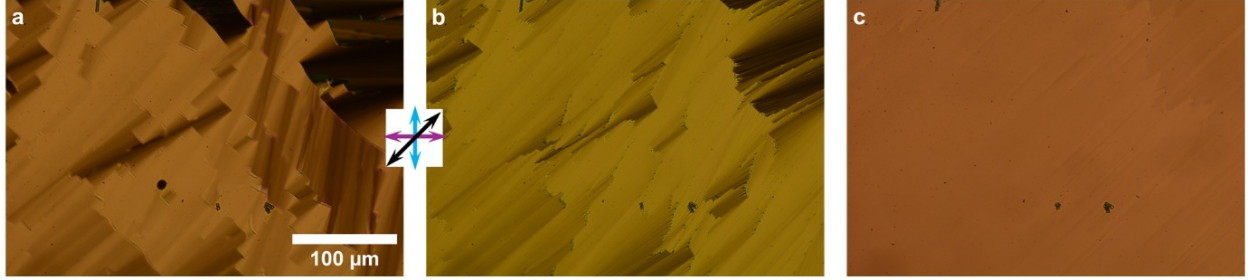


FIG. S1. POM images of compound **1** in a 5 μm thick parallel rubbed planar cell at a) 120 $^{\circ}\text{C}$ in the SmA_{F} phase on heating, b) 150 $^{\circ}\text{C}$ in the SmA phase on heating and c) 120 $^{\circ}\text{C}$ in the SmA_{F} phase on cooling. The blue and purple arrows indicate the polariser axes while the black arrow indicates the rubbing direction.

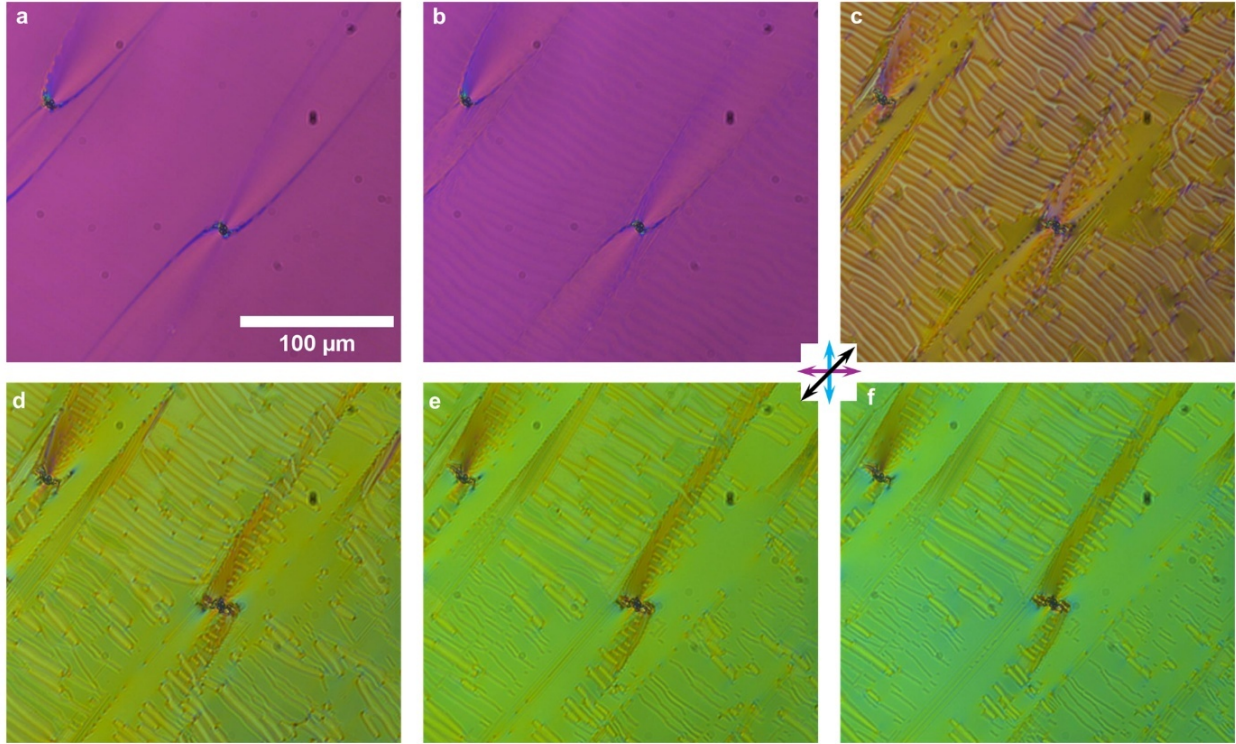


FIG. S2. POM images of compound **2** in a 5 μm thick parallel rubbed planar cell at a) 105 $^{\circ}\text{C}$ in the N_{F} phase on cooling and b) 104 $^{\circ}\text{C}$, c) 103 $^{\circ}\text{C}$, d) 102 $^{\circ}\text{C}$ e) 101 $^{\circ}\text{C}$ and f) 100 $^{\circ}\text{C}$ in the $\text{N}_{\text{TB}_{\text{F}}}$ phase on cooling. The blue and purple arrows indicate the polariser axes while the black arrow indicates the rubbing direction.

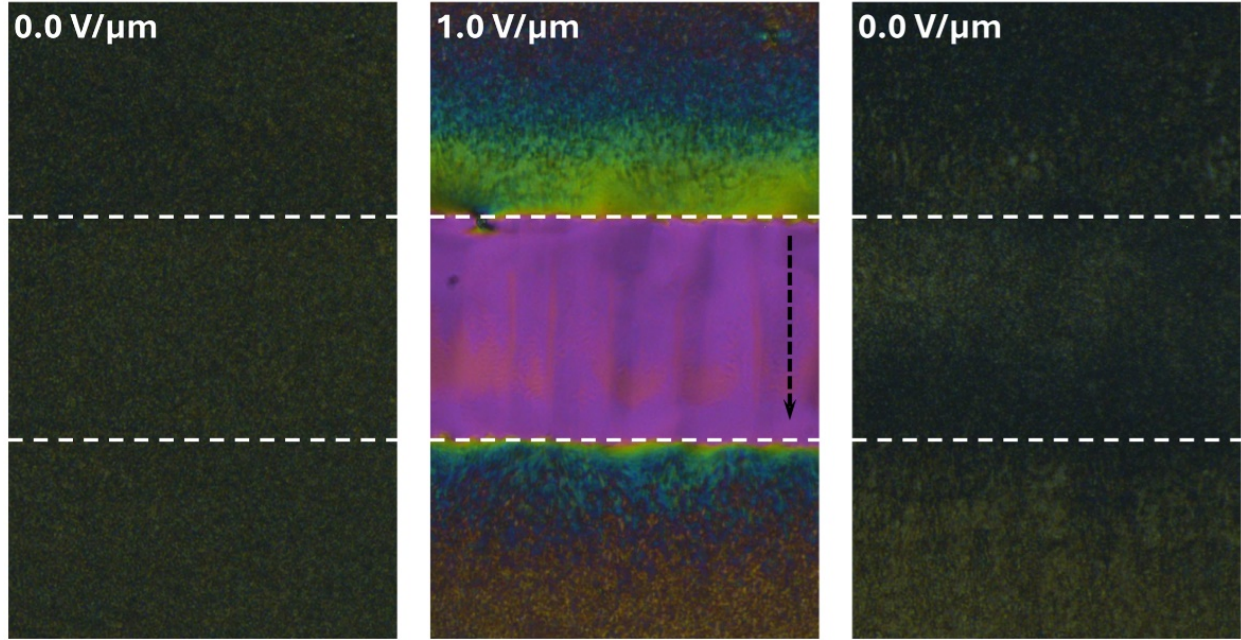


FIG. S3. POM observations of compound **2** in the $\text{SmC}_\text{P}^\text{H}$ phase at 92 °C in a 5.5 μm parallel rubbed planar aligned cell with a pair of in plane electrodes separated by 100 μm . Voltage is applied OFF-ON-OFF.

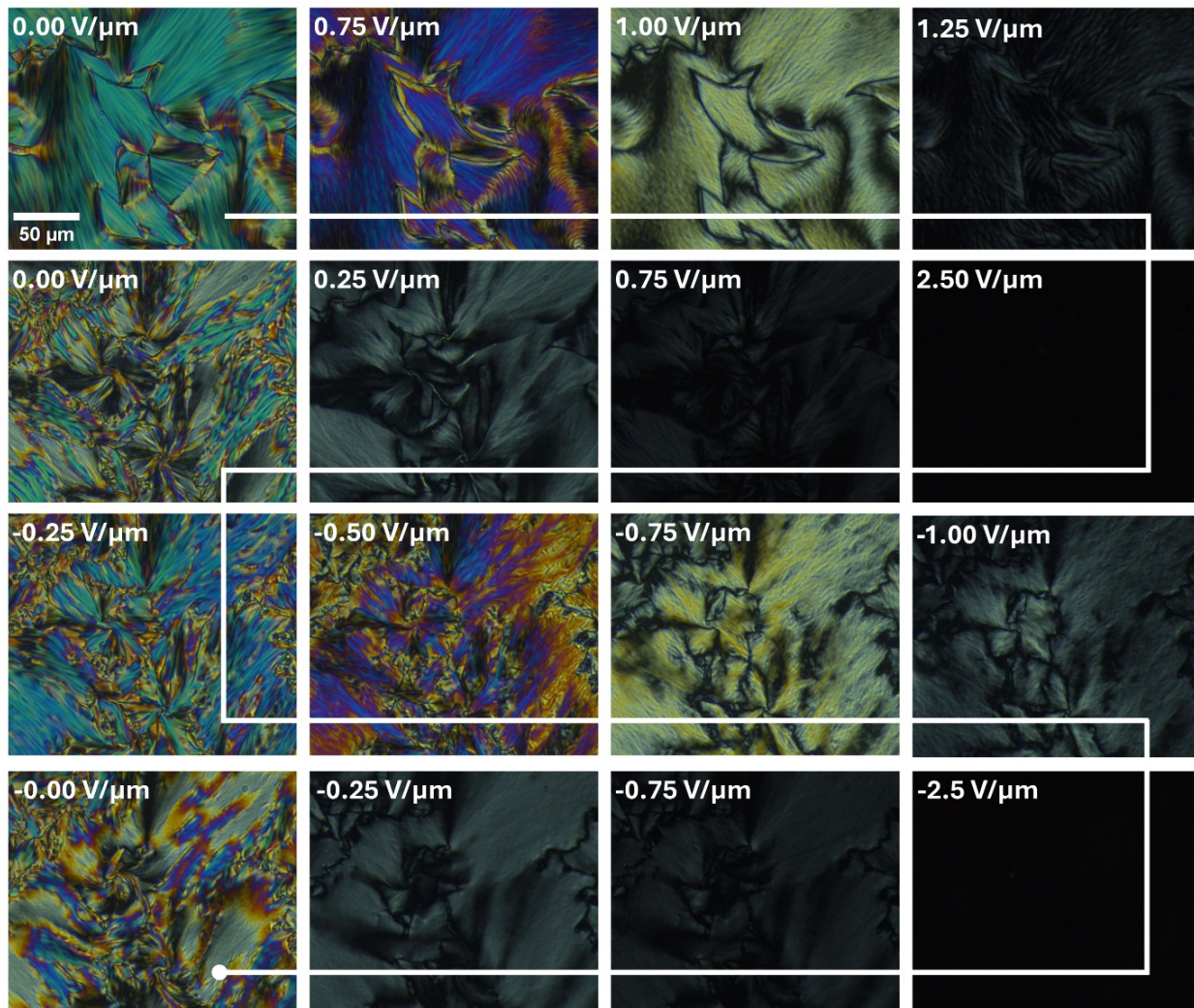


FIG. S4. POM observations of compound **1** in the SmC_P^H phase at 70 °C in a 4 μm cell with no alignment layer. Field strength values indicate the strength of DC field applied across the cell gap.

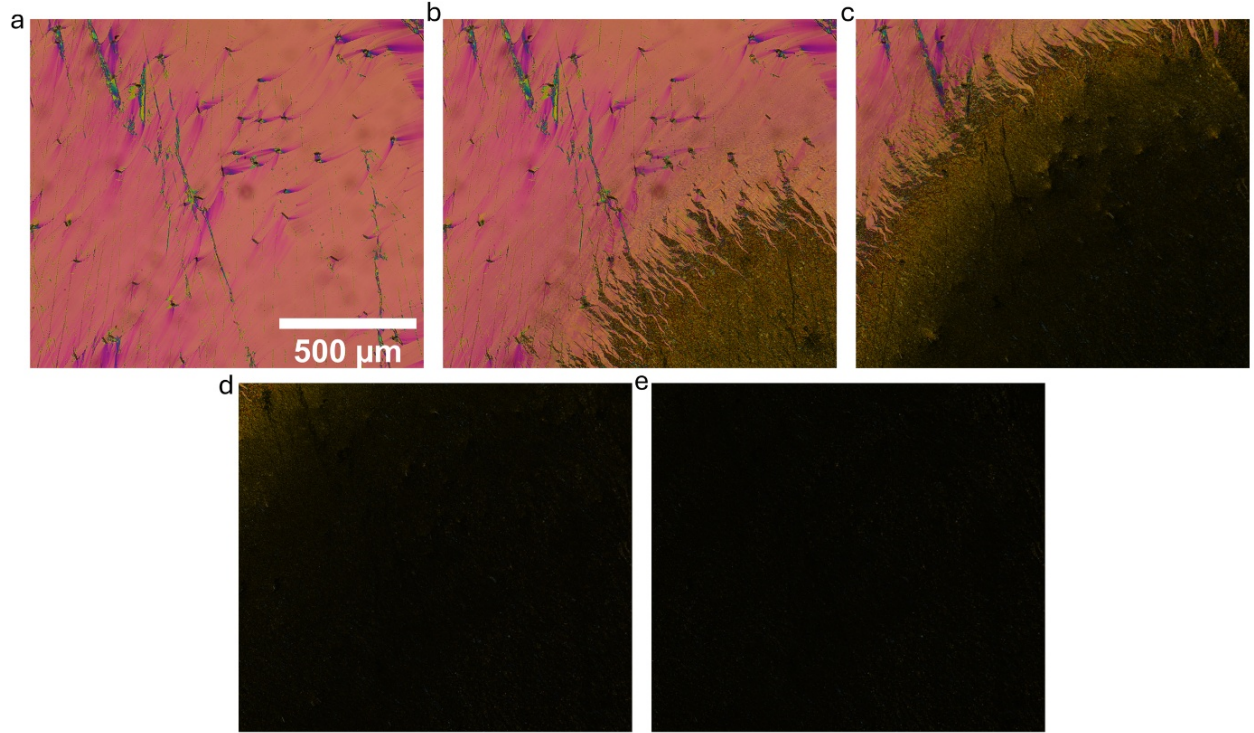


FIG. S5. POM observations of **3** at the boundary between the N_F and SmC_P^H phases over $1\text{ }^\circ\text{C}$ showing the slow growth and dendritic tendrils.

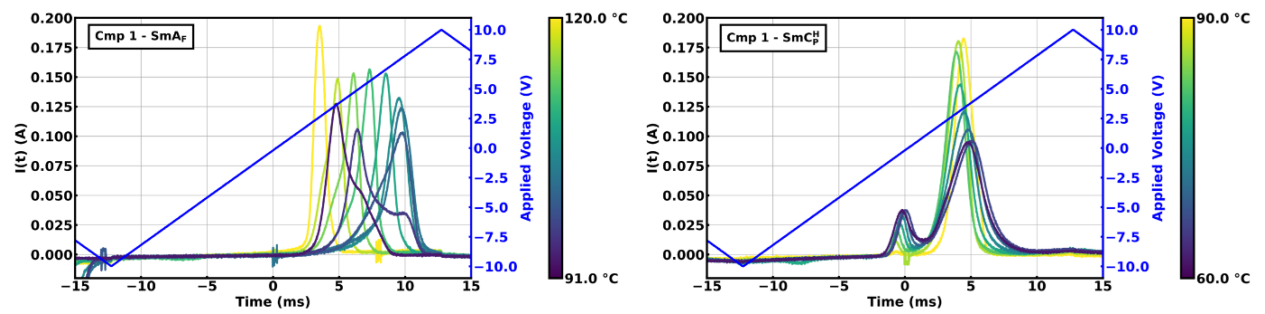
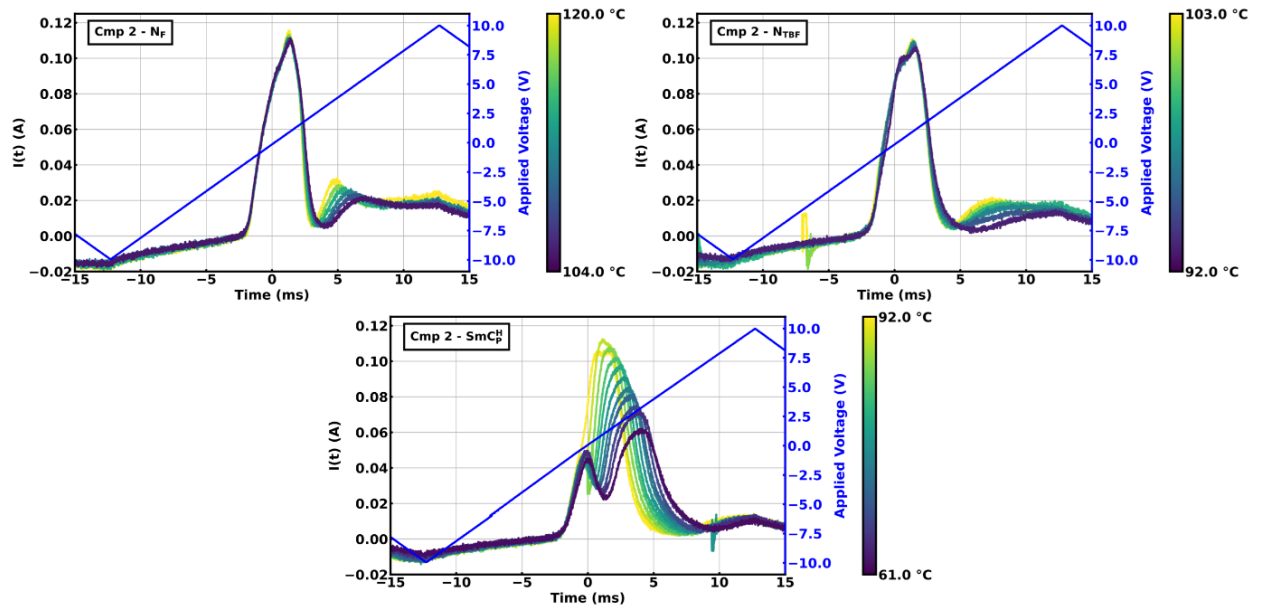
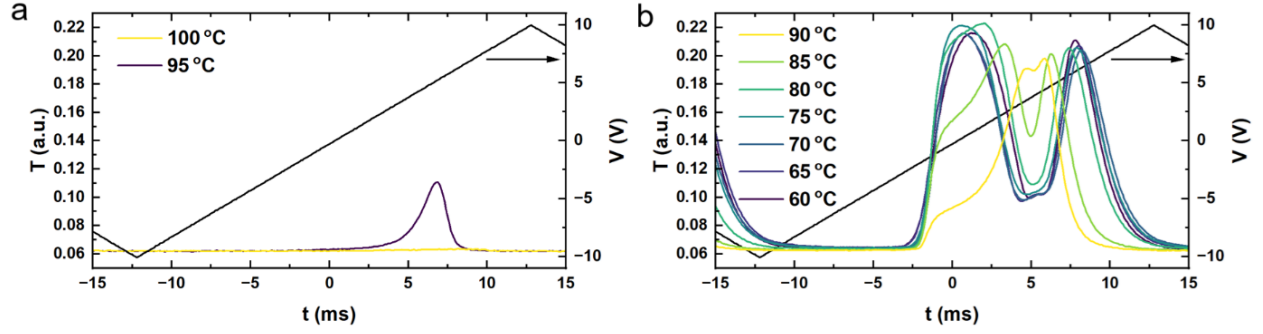


FIG. S6. Current responses for compound **1** in a $4\text{ }\mu\text{m}$ cell with no alignment layer. The applied field is a triangle wave with 10 V ($2.5\text{ V}/\mu\text{m}$) at 10 Hz .



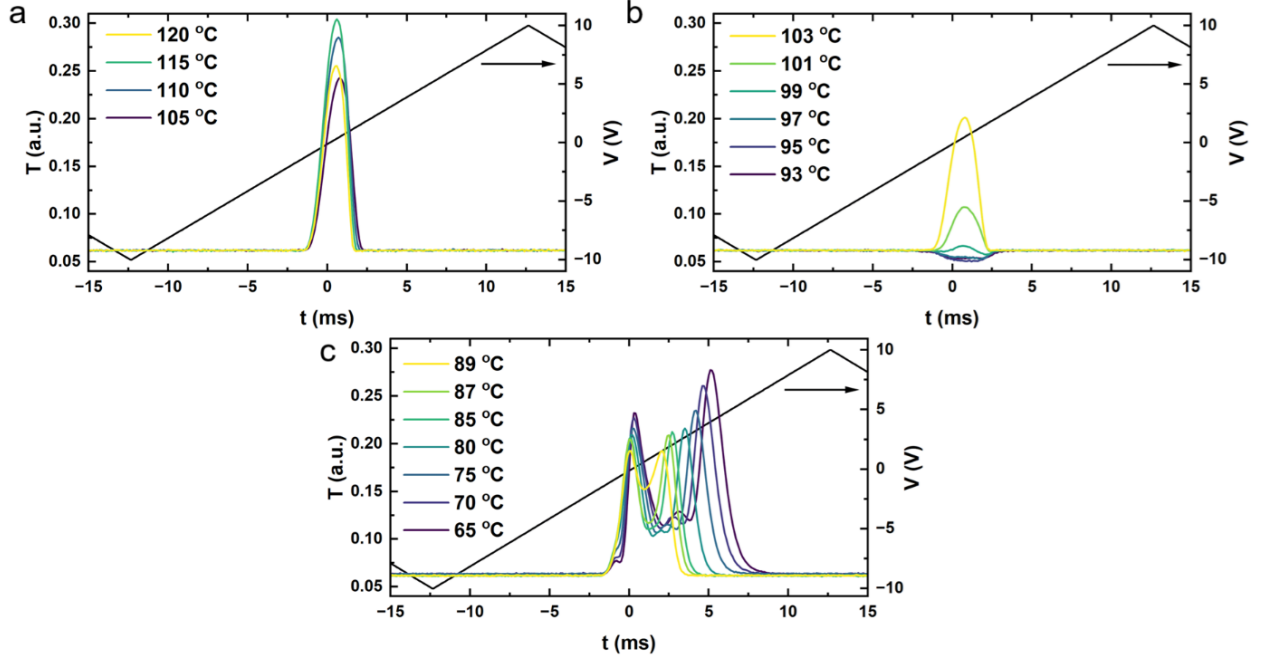


FIG. S9. Electro-optic response for compound **2** in a 4 μm cell with no alignment layer set between crossed polarisers. The applied field is a triangle wave with 10 V (2.5 V/ μm) at 10 Hz.

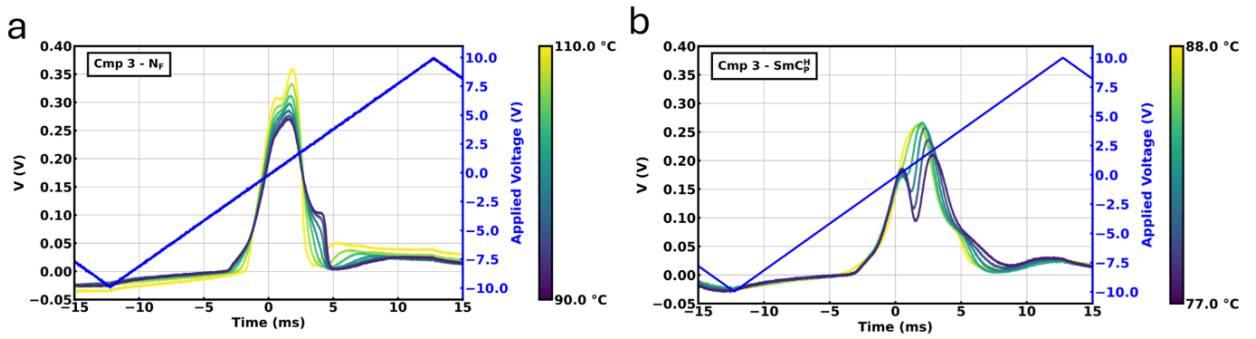


FIG. S10. Current responses for compound **3** in a 4 μm cell with no alignment layer. The applied field is a triangle wave with 10 V (2.5 V/ μm) at 10 Hz

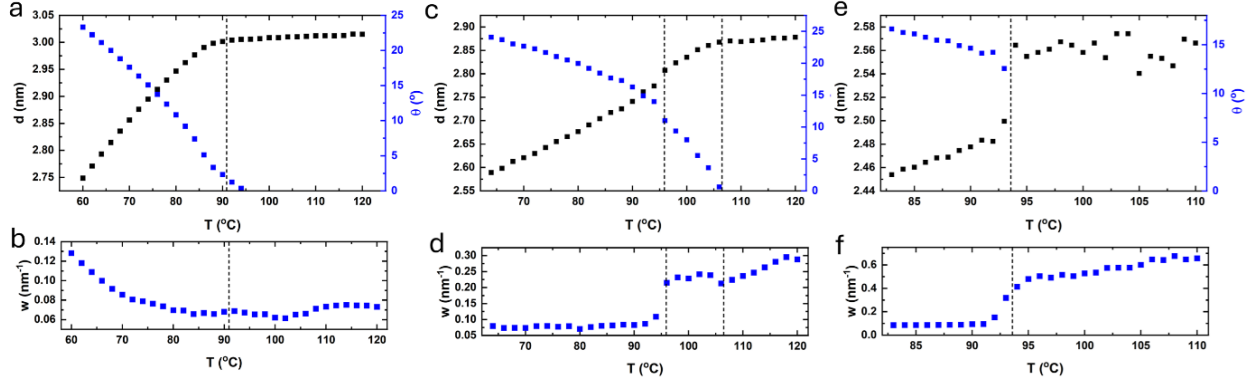


FIG. S11. Temperature dependence and FWHM of the small angle scattering peaks of a,b) **1**, c,d) **2** and e,f) **3**.

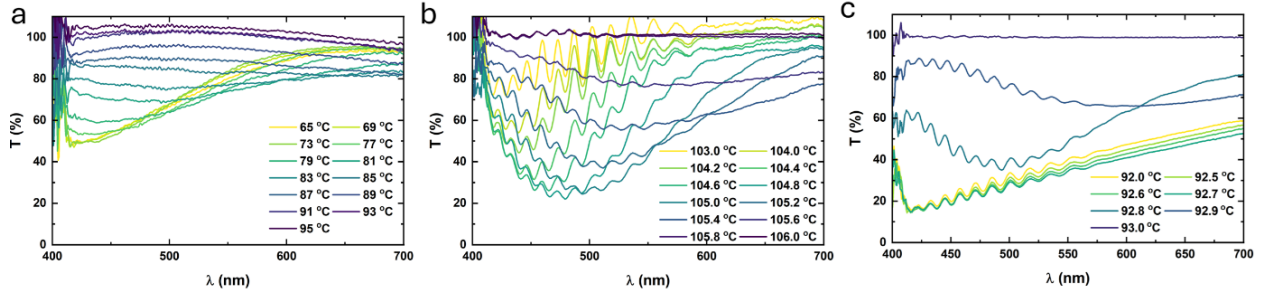


FIG. S12. Transmission spectrum of a) **1** b) **2** and c) **3**. For all samples the wavelength shifts to shorter wavelengths.

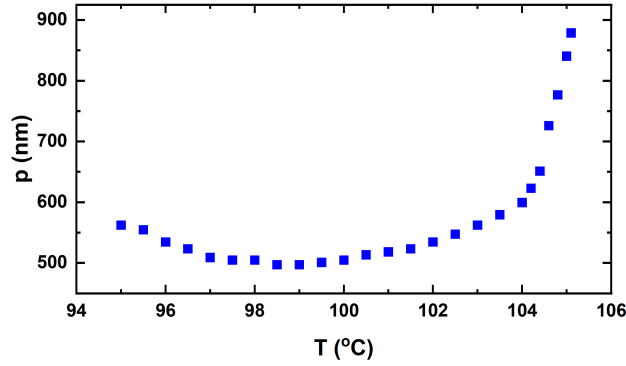


FIG. S13. Temperature dependence of the pitch of **2** in the N_{TBF} phase obtained on cooling in a $5\ \mu\text{m}$ parallel rubbed planar cell.

3. ORGANIC SYNTHESIS

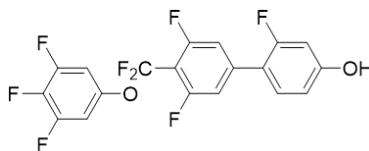
The synthetic route and chemical characterisation data associated with intermediate products and materials **2-4** is given below. The synthesis of material **1** and the preparation of 2,6-difluoro-4-(5-propyl-1,3-dioxan-2-yl)benzoic acid is reported elsewhere [1,2]

3.1. General Suzuki Coupling Protocol

A reaction flask was charged with 5-bromo-2-(difluoro(3,4,5-trifluorophenoxy)methyl)-1,3-difluorobenzene (20 mmol) and the relevant phenol boronic ester (21 mmol) which were dissolved in 150 mL of THF and 60 mL of 2M K₂CO₃(aq). The resultant solution was sparged with N_{2(g)} for 20 mins. In a separate vial, 5 mL of THF was sparged with N_{2(g)} for 15 minutes before Pd(OAc)₂ (50 mg) and SPhos (100 mg) were added and stirred for a further 5 mins. The reaction flask was then heated to 70 °C and the catalyst solution added in one portion. The reaction was monitored by TLC with the completion of the reaction being determined by the complete consumption of the bromo-sub-straight. The reaction was then cooled, the aqueous and organic layers separated with the organics being dried over MgSO₄. The organics were then passed through a silica plug before the filtrate was concentrated under reduced pressure and purified by flash chromatography over silica gel with a gradient of hexane/ethyl acetate using a Combiflash NextGen300+ system using a gradient elution from hexane - ethyl acetate. Finally, the product re-crystallised from hexane:toluene (10:1) to give the appropriate phenols.

Insert scheme here

Scheme 1. General Suzuki coupling protocol.



4-Hydroxy-5-(2-fluoro-4-hydroxyphenyl)-2-(difluoro(3,4,5-trifluorophenoxy)methyl)-1,3-difluorobenzene

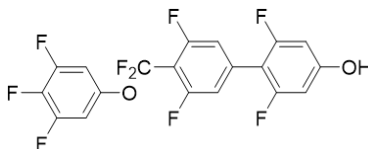
Appearance: White powder

R_f (DCM): 0.35

^1H NMR (400 MHz, DMSO) (δ): 10.38 (s, 1H, Ar-OH), 7.50 (t, $J = 8.5$ Hz, 1H, Ar-H), 7.47 – 7.42 (m_{apparent} , 2H, Ar-H), 7.42 – 7.32 (m_{apparent} , 2H, Ar-H), 6.77 – 6.67 (m_{apparent} , 2H, Ar-H).

$^{13}\text{C}\{^1\text{H}\}$ NMR (101 MHz, DMSO) (δ): 160.43 (d, $J = 249.3$ Hz), 159.97 (d, $J = 248.2$ Hz), 157.76 (d, $J = 6.2$ Hz), 150.26 (ddd, $J = 248.7, 10.5, 5.1$ Hz), 144.17 (t, $J = 16.3$ Hz), 142.08 (t, $J = 11.4$ Hz), 137.83 (d, $J = 248.3$ Hz), 131.32, 122.63, 120.00, 117.38, 115.07 (d, $J = 11.9$ Hz), 112.71, 112.49, 108.10 – 107.67 (m_{apparent}), 106.45 (t, $J = 13.3$ Hz), 103.26 (d, $J = 24.6$ Hz).

^{19}F NMR (376 MHz, DMSO) (δ): -60.40 (t, $J = 25.7$ Hz, 2F, O-CF₂-Ar), -111.61 (td, $J = 26.5, 13.0$ Hz, 2F, Ar-F), -115.39 (t, $J = 11.0$ Hz, 1F, Ar-F), -132.89 (dd, $J = 22.0, 9.2$ Hz, 2F, Ar-F), -163.29 (tt, $J = 22.2, 6.0$ Hz, 1F, Ar-F).



4-Hydroxy-5-(2,6-difluoro-4-(difluoromethoxy)phenyl)-2-(difluoro(3,4,5-trifluorophenoxy)methyl)- 1,3-difluorobenzene

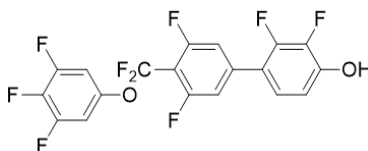
Appearance: White powder

R_f (DCM): 0.40

^1H NMR (400 MHz, DMSO) (δ): 10.79 (s, 1H, Ar-OH), 7.44 – 7.35 (m, 4H, Ar-H)*, 6.61 (ddd, $J = 10.2, 2.8$ Hz, 2H, Ar-H). (*Overlapping signals)

$^{13}\text{C}\{^1\text{H}\}$ NMR (101 MHz, DMSO) (δ): 161.00 (dd, $J = 246.2, 10.0$ Hz), 160.41 – 159.89 (m_{apparent}), 157.49 (d, $J = 5.9$ Hz), 150.27 (ddd, $J = 248.9, 10.6, 5.3$ Hz), 144.50 – 143.68 (m_{apparent}), 137.87 (dt, $J = 248.3, 15.3$ Hz), 136.06 (t, $J = 11.9$ Hz), 122.49, 119.86, 117.48 – 116.99 (m_{apparent}), 115.02, 114.75, 108.02, 107.78, 105.24 (t, $J = 18.6$ Hz), 99.83, 99.56.

^{19}F NMR (376 MHz, DMSO) (δ): -60.71 (t, $J = 26.0$ Hz, 2F, O-CF₂-Ar), -111.79 (td, $J = 26.0, 11.7$ Hz, 2F, Ar-F), -114.54 (d, $J = 10.8$ Hz, 2F, Ar-F), -132.92 (dd, $J = 22.0, 9.1$ Hz, 2F, Ar-F), -163.29 (tt, $J = 22.0, 6.1$ Hz, 1F, Ar-F).



4-Hydroxy-5-(2,3-difluoro-4-hydroxyphenyl)-2-(difluoro(3,4,5-trifluorophenoxy)methyl)- 1,3-difluorobenzene

Appearance: White powder

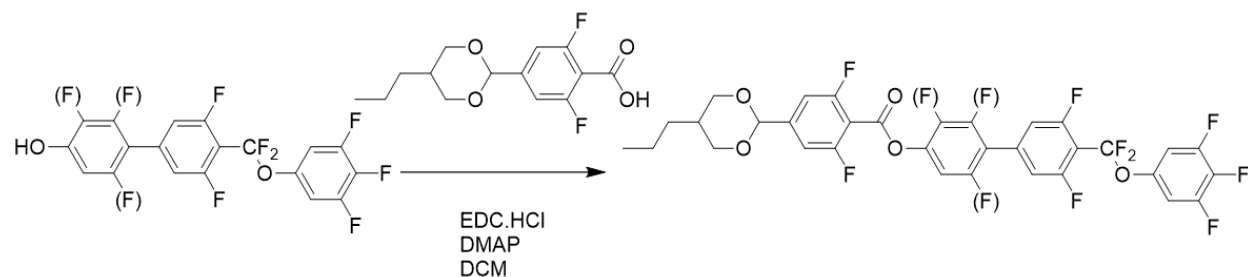
R_f (DCM): 0.33

¹H NMR (400 MHz, DMSO) (δ): 10.90 (s, 1H, Ar-OH), 7.51 (d_{apparent}, J = 11.5 Hz, 2H, Ar-H), 7.47 – 7.37 (m_{apparent}, 2H, Ar-H), 7.32 (td, J = 8.7, 2.2 Hz, 1H, Ar-H), 6.90 (td, J = 8.0, 1.9 Hz, 1H, Ar-H).

¹³C NMR (101 MHz, DMSO) δ 159.48 (dd, J = 255.2, 6.9 Hz), 151.89 (ddd, J = 248.0, 10.8, 5.3 Hz), 150.15 (dd, J = 239.6, 11.1 Hz), 148.45 (d, J = 6.9 Hz), 144.59 (t, J = 12.3 Hz), 141.54 (t, J = 15.0 Hz), 139.20 (d, J = 14.4 Hz), 137.09 (t, J = 15.7 Hz), 124.97 (t, J = 3.5 Hz), 116.89 (d, J = 10.6 Hz), 113.81 (t, J = 2.3 Hz), 113.39 (dt, J = 24.2, 3.4 Hz), 108.40 (dd, J = 23.8, 6.5 Hz), 107.53 (t, J = 6.2 Hz).

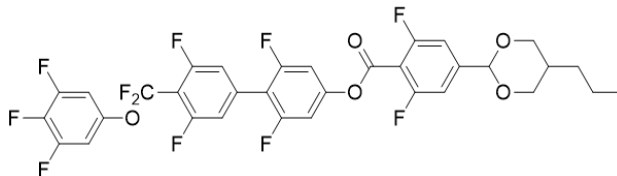
¹⁹F NMR (376 MHz, DMSO) (δ): -60.43 (t, J = 25.6 Hz, 2F, O-CF₂-Ar), -111.20 (td, J = 25.8, 11.9 Hz, 2F, Ar-F), -132.84 (dd, J = 22.1, 9.3 Hz, 2F, Ar-F), -141.59 (dd, J = 20.5, 8.4 Hz, 1F, Ar-F), -160.90 (dd, J = 20.6, 8.0 Hz, 1F, Ar-F), -163.17 (tt, J = 22.3, 5.4 Hz, 1F, Ar-F).

3.2. General Esterification Protocol

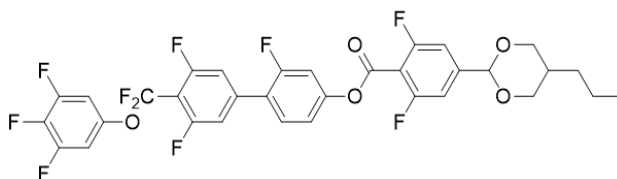


Scheme 2. General esterification protocol used in the preparation of compounds **2-4**.

The 2,6-difluoro-4-(5-propyl-1,3-dioxan-2-yl)benzoic acid (1.5 mmol), the relevant phenol (1 mmol), EDC.HCl (1.5 mmol), DMAP (5 mg) were weighed into a reaction vial or round bottom flask. DCM was added (~ 10 ml, final concentration w.r.t. phenol ~ 0.1 M), and the resulting suspension stirred until complete consumption of the starting phenol as judged by TLC. The crude reaction mixture was purified by flash chromatography using a 12 g SiO₂ cartridge as the stationary phase and a gradient of hexane/DCM (0% DCM - 100% DCM)



as the mobile phase, with detection made in the range 200-800 nm. The chromatographed material was filtered through a 200 nm PTFE syringe filter, concentrated to dryness, and finally recrystallised from ethanol.



2

Yield: (white crystals) 516 mg, 75%

R_f (DCM): 0.91

¹H NMR (400 MHz, CDCl₃) (δ): 7.49 (t, *J* = 8.6 Hz, 1H, Ar-**H**), 7.26 – 7.16 (m, 6H, Ar-**H**)*, 7.04 – 6.95 (m_{apparent}, 2H, Ar-**H**), 5.40 (s, 1H, Ar-CH-O₂), 4.26 (dd, *J* = 11.8, 4.7 Hz, 2H, O-CH_{ax}(H_{eq})-CH), 3.54 (t, *J* = 11.2 Hz, 2H, O-CH_{eq}(H_{ax})-CH), 2.21 – 2.08 (m_{apparent}, 1H, (CH₂)₂-CH-CH₂), 1.35 (h, *J* = 7.6 Hz, 2H, CH₂-CH₂-CH₃), 1.11 (q, *J* = 7.6 Hz, 2H, CH-CH₂-CH₂-CH₃), 0.94 (t, *J* = 7.3 Hz, 3H, CH₂-CH₃). (*Overlapping Signals)

¹³C{¹H} NMR (101 MHz, CDCl₃) (δ): 162.21 (dd, *J* = 248.9, 6.1 Hz), 161.27 (d_{apparent}, *J* = 260.9 Hz), 159.56 (d, *J* = 253.7 Hz), 151.58 (d, *J* = 11.8 Hz), 151.03 (dt, *J* = 259.7, 10.9 Hz), 145.74 (t, *J* = 9.5 Hz), 144.59 (t, *J* = 14.8 Hz), 140.67 (t, *J* = 12.9 Hz), 130.62 (d, *J* = 3.7 Hz), 123.71 (d, *J* = 13.6 Hz), 120.15, 118.35 (d, *J* = 3.8 Hz), 113.14 (dt, *J* = 24.4, 3.1 Hz), 110.84 (d, *J* = 26.0 Hz), 110.33 (dd, *J* = 23.9, 2.8 Hz), 109.33 (d, *J* = 16.2 Hz), 107.48 (m_{apparent}), 98.79 (t, *J* = 2.2 Hz), 72.60, 33.90, 30.23, 19.53, 14.19.

¹⁹F NMR (376 MHz, CDCl₃) (δ): -61.78 (t, *J* = 26.3 Hz, 2F, O-CF₂-Ar), -108.41 (d, *J* = 9.6 Hz, 2F, Ar-F), -110.33 (td, *J* = 26.4, 11.1 Hz, 2F, Ar-F), -113.60 (t, *J* = 9.6 Hz, 1F, Ar-F), -132.43 (dd, *J* = 20.6, 8.7 Hz, 2F, Ar-F), -163.11 (tt, *J* = 20.8, 5.6 Hz, 1F, Ar-F)

HPLC (C18): 99.68 % (254 nm, 6.047 min)

HRMS (ESI +, *m/z*) = [*m*+Na]⁺: Calculated for C₃₃H₂₂F₁₀O₅Na: 711.1200, found 711.1182 (error = 2.5 ppm)

3

Yield: (white crystals) 502 mg, 71 %

R_f (DCM): 0.88

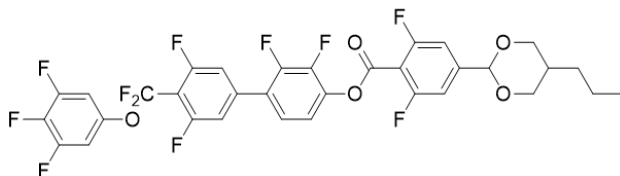
¹H NMR (400 MHz, CDCl₃) (δ): 7.20 (d_{apparent}, J = 10.1 Hz, 2H, Ar-**H**), 7.16 (d_{apparent}, J = 10.4 Hz, 2H, Ar-**H**), 7.09 – 6.94 (m, 4H, Ar-**H**)*, 5.40 (s, 1H, Ar-CH-O₂), 4.26 (dd, J = 11.8, 4.6 Hz, 2H, O-CH_{ax}(H_{eq})-CH), 3.54 (t, J = 11.3 Hz, 2H, O-CH_{eq}(H_{ax})-CH), 2.21 – 2.07 (m_{apparent}, 1H, (CH₂)₂-CH-CH₂), 1.35 (h, J = 7.4 Hz, 2H, CH₂-CH₂-CH₃), 1.11 (q, J = 7.0 Hz, 2H, CH-CH₂-CH₂-CH₃), 0.94 (t, J = 7.3 Hz, 3H, CH₂-CH₃). (*Overlapping Signals)

¹³C{¹H} NMR (101 MHz, CDCl₃) (δ): 162.32 (dd, J = 258.5, 5.7 Hz), 161.00, 160.23 (dd, J = 251.6, 7.8 Hz), 158.79, 152.36 (ddd, J = 251.1, 10.3, 5.6 Hz), 151.38 (t, J = 14.3 Hz), 146.05 (t, J = 9.7 Hz), 139.76 (t, J = 14.0 Hz), 134.28 (t, J = 10.0 Hz), 122.68, 120.02, 117.38, 114.76 (d, J = 24.7 Hz), 110.36 (dd, J = 23.6, 3.5 Hz), 108.91, 107.75 – 107.29 (m_{apparent}), 106.97 – 106.47 (m_{apparent}), 98.73 (t, J = 2.0 Hz), 72.60, 33.90, 30.22, 19.53, 14.18.

¹⁹F NMR (376 MHz, CDCl₃) (δ): -61.95 (t, J = 26.5 Hz, 2F, O-CF₂-Ar), -108.15 (d, J = 10.0 Hz, 2F, Ar-F), -110.53 (td, J = 26.5, 10.7 Hz, 2F, Ar-F), -111.71 (d, J = 9.1 Hz, 2F, Ar-F), -132.43 (dd, J = 20.9, 8.6 Hz, 2F, Ar-F), -163.07 (tt, J = 20.7, 5.9 Hz, 1F, Ar-F).

HPLC (C18): 99.58 % (254 nm, 6.060 min)

HRMS (ESI +, m/z) = [m+Na]⁺: Calculated for C₃₃H₂₁F₁₁O₅Na: 729.1106, found 729.1101 (error = 0.7 ppm)



4

Yield: (white crystals) 435 mg, 62 %

R_f (DCM): 0.90

¹H NMR (400 MHz, CDCl₃) (δ): 7.29 – 7.16 (m, 6H, Ar-**H**)*[†], 7.00 (dd, J = 7.9, 5.8 Hz, 2H, Ar-**H**), 5.41 (s, 1H, Ar-CH-O₂), 4.26 (dd, J = 11.7, 4.6 Hz, 2H, O-CH_{ax}(H_{eq})-CH), 3.54 (t, J = 11.4 Hz, 2H, O-CH_{eq}(H_{ax})-CH), 2.21 – 2.07 (m_{apparent}, 1H, (CH₂)₂-CH-CH₂), 1.35

(h, $J = 7.7$ Hz, 2H, CH₂-CH₂-CH₃), 1.11 (q, $J = 7.1$ Hz, 2H, CH-CH₂-CH₂-CH₃), 0.94 (t, $J = 7.3$ Hz, 3H, CH₂-CH₃). (*Overlapping peaks, †Overlapping CDCl₃ peak)

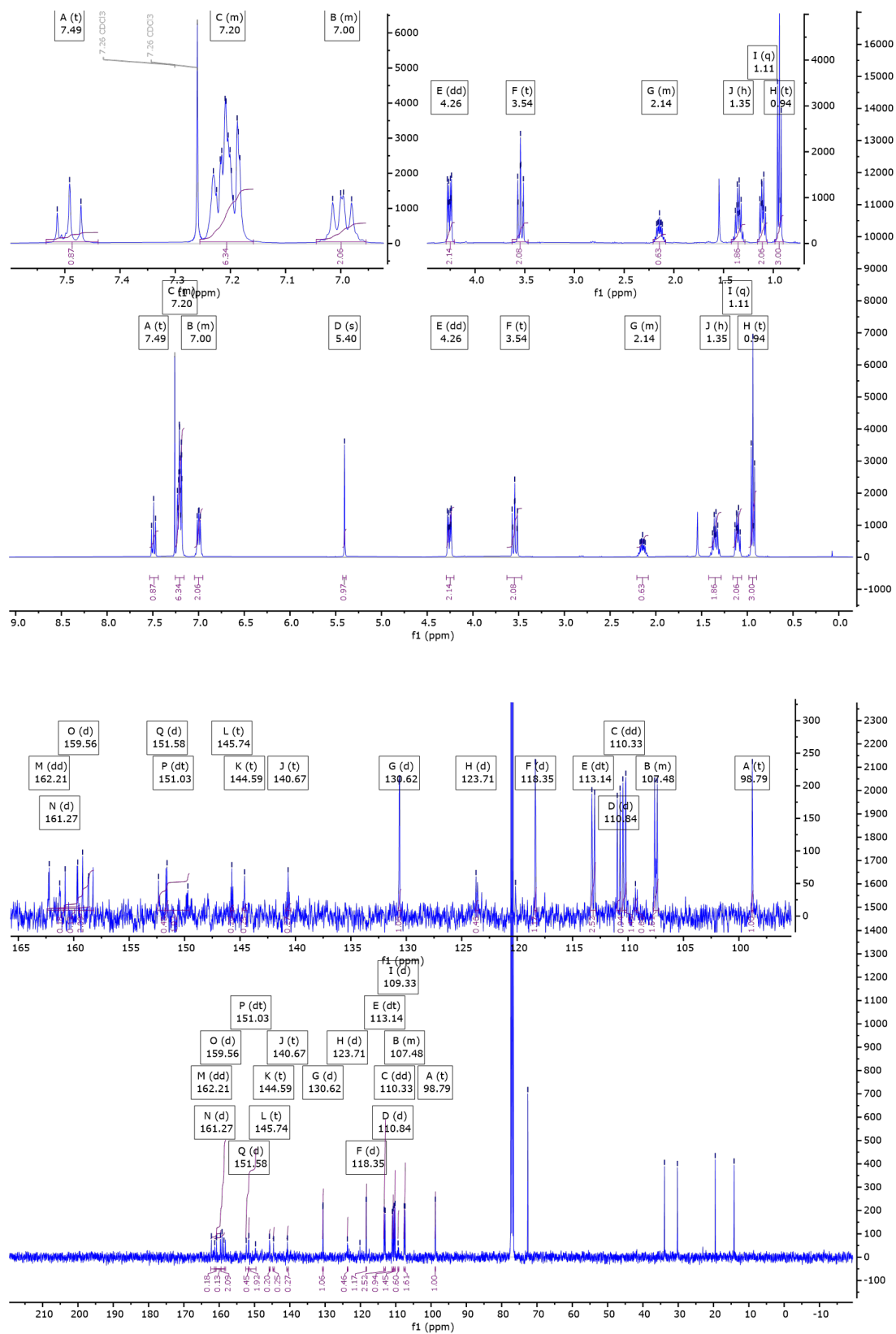
¹³C{¹H} NMR (101 MHz, CDCl₃) (δ): 162.43 (dd, $J = 259.8, 5.4$ Hz), 161.34 (dd, $J = 259.2, 6.3$ Hz), 158.22, 150.82 (ddd, $J = 250.5, 10.6, 5.1$ Hz), 150.03, 147.45 (dd, $J = 245.7, 12.0$ Hz), 146.18 (t, $J = 9.9$ Hz), 144.85 – 144.33 (m_{apparent}), 142.49 (d, $J = 15.0$ Hz), 140.04 – 139.30 (m_{apparent}), 137.35 (t, $J = 15.1$ Hz), 125.49 (d, $J = 9.5$ Hz), 123.73 (t, $J = 4.0$ Hz), 122.69, 120.04, 119.15 (d, $J = 4.0$ Hz), 113.14 (dt, $J = 24.7, 3.3$ Hz), 110.38 (dd, $J = 23.5, 3.5$ Hz), 109.58 (t, $J = 14.3$ Hz), 108.43 (t, $J = 16.8$ Hz), 107.80 – 107.30 (m_{apparent}), 98.73 (t, $J = 1.6$ Hz), 72.58, 33.90, 30.22, 19.53, 14.16.

¹⁹F NMR (376 MHz, CDCl₃) (δ): -61.87 (t, $J = 26.4$ Hz, 2F, O-CF₂-Ar), -107.59 (d, $J = 10.0$ Hz, 2F, Ar-F), -109.76 (td, $J = 26.5, 10.7$ Hz, 2F, Ar-F), -132.40 (dd, $J = 20.7, 8.7$ Hz, 2F, Ar-F), -138.63 (dd, $J = 20.1, 6.5$ Hz, 1F, Ar-F), -147.62 (dd, $J = 20.3, 5.6$ Hz, 1F, Ar-F), -163.04 (tt, $J = 21.0, 5.0$ Hz, 1F, Ar-F).

HPLC (C18): 99.81 % (254 nm, 6.061 min)

HRMS (ESI +, m/z) = [m+Na]⁺: Calculated for C₃₃H₂₁F₁₁O₅Na: 729.1106, found 729.1101 (error = 0.6 ppm)

3.3. Example NMR Spectra, HPLC Chromatograms, and HRMS Spectra.



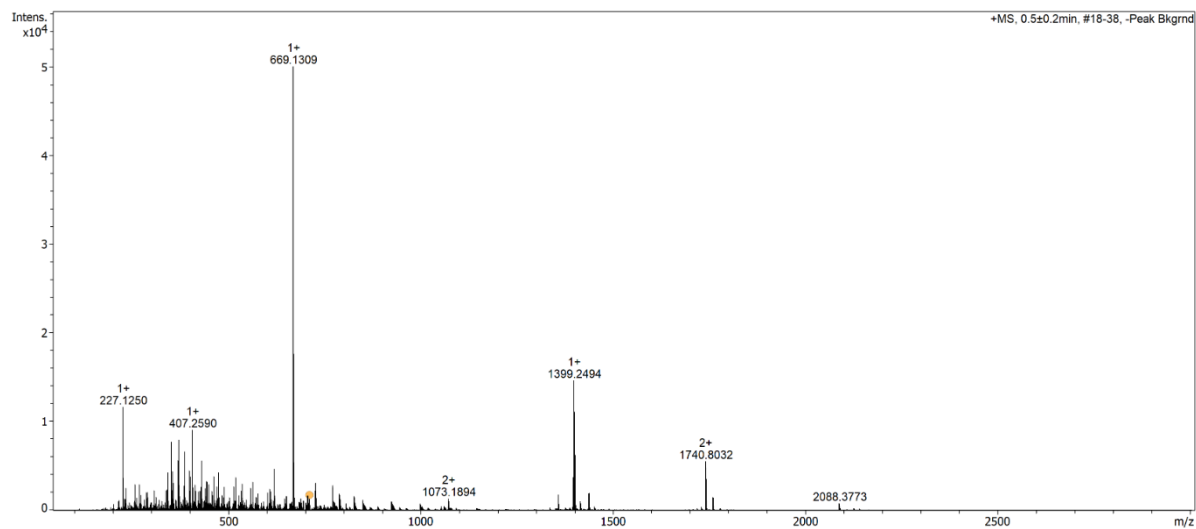
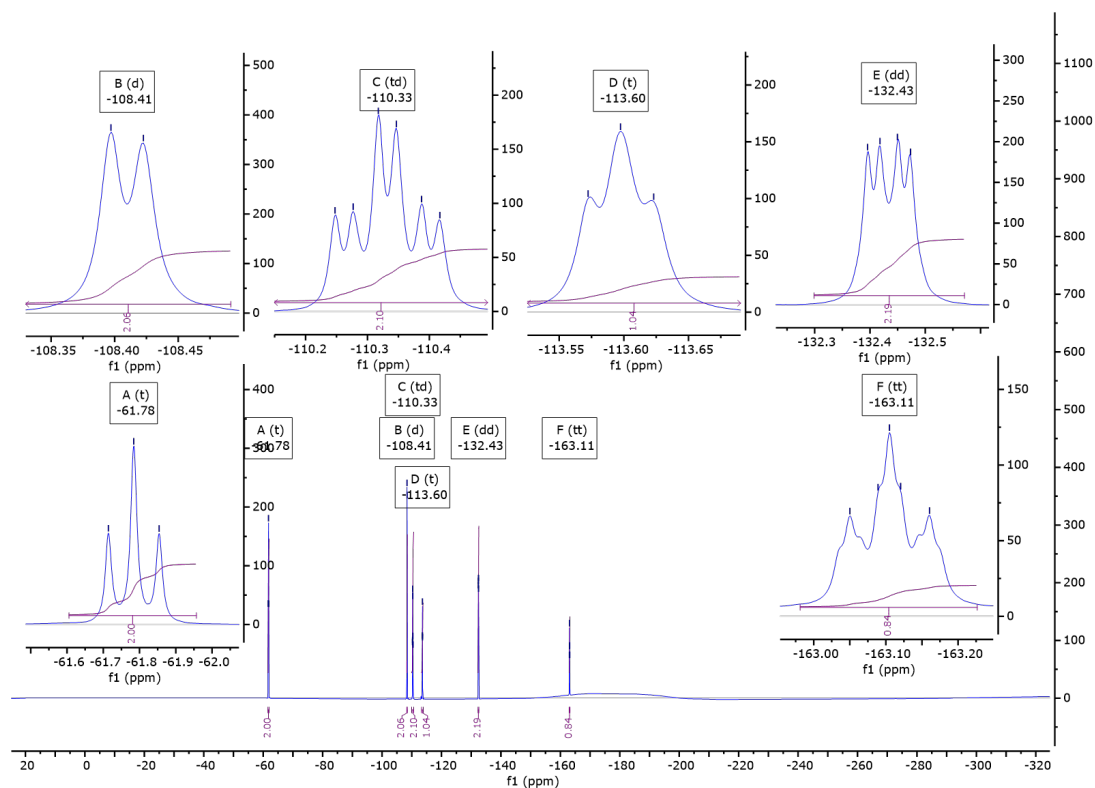
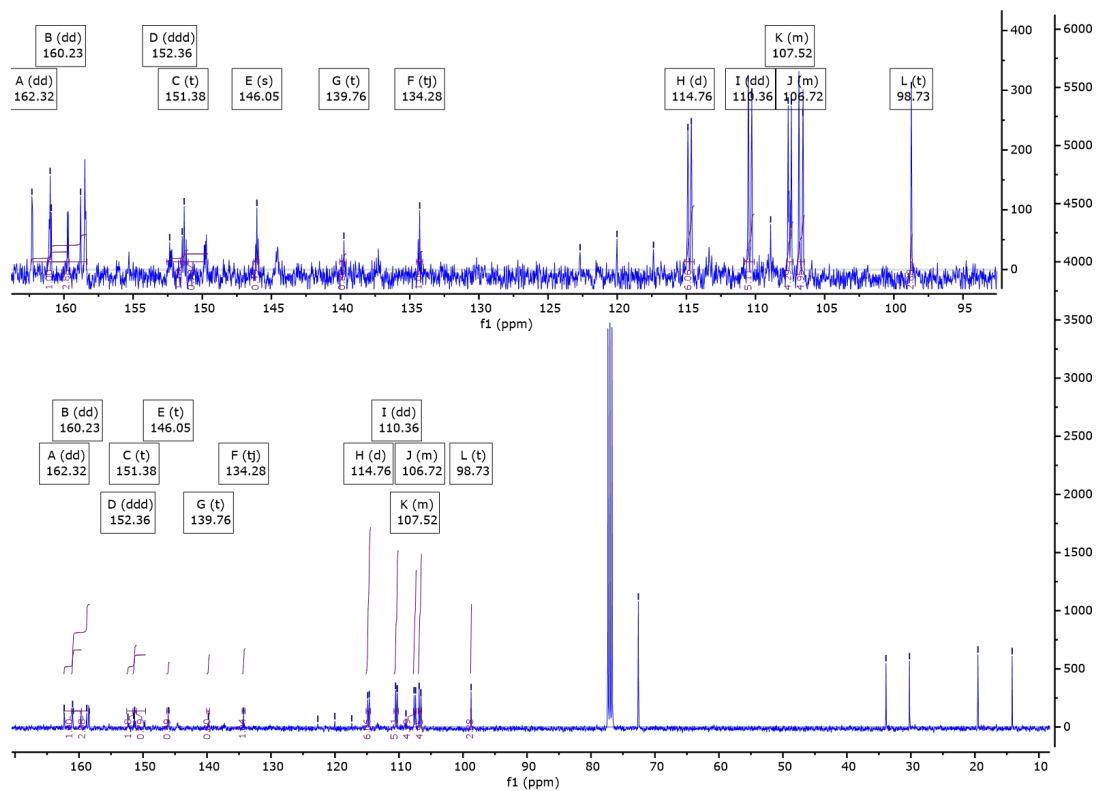
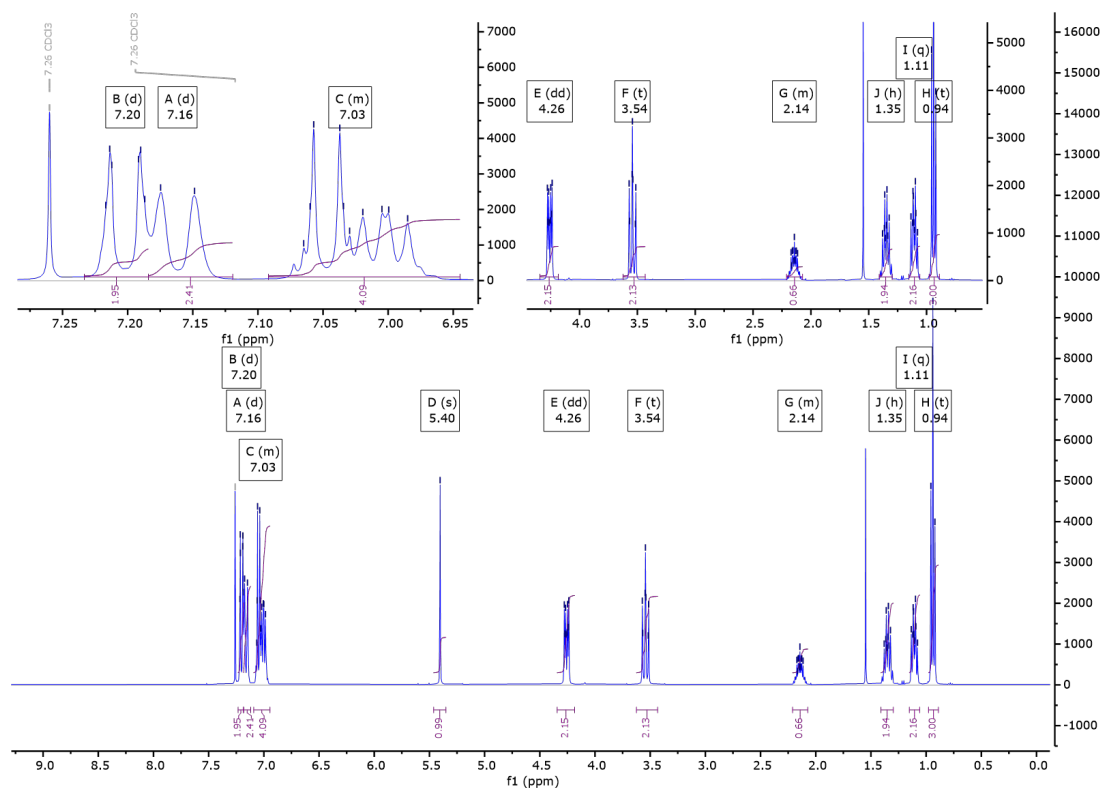


Fig. S14. ^1H [top], $^{13}\text{C}\{^1\text{H}\}$ [middle], and ^{19}F [bottom] NMR spectra, and HRMS Spectra for **2**.



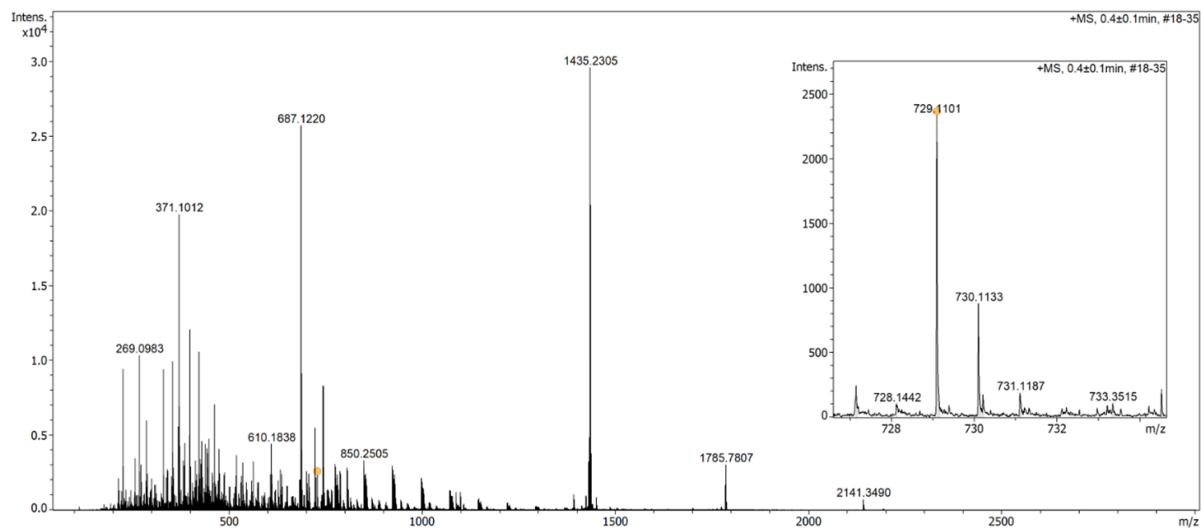
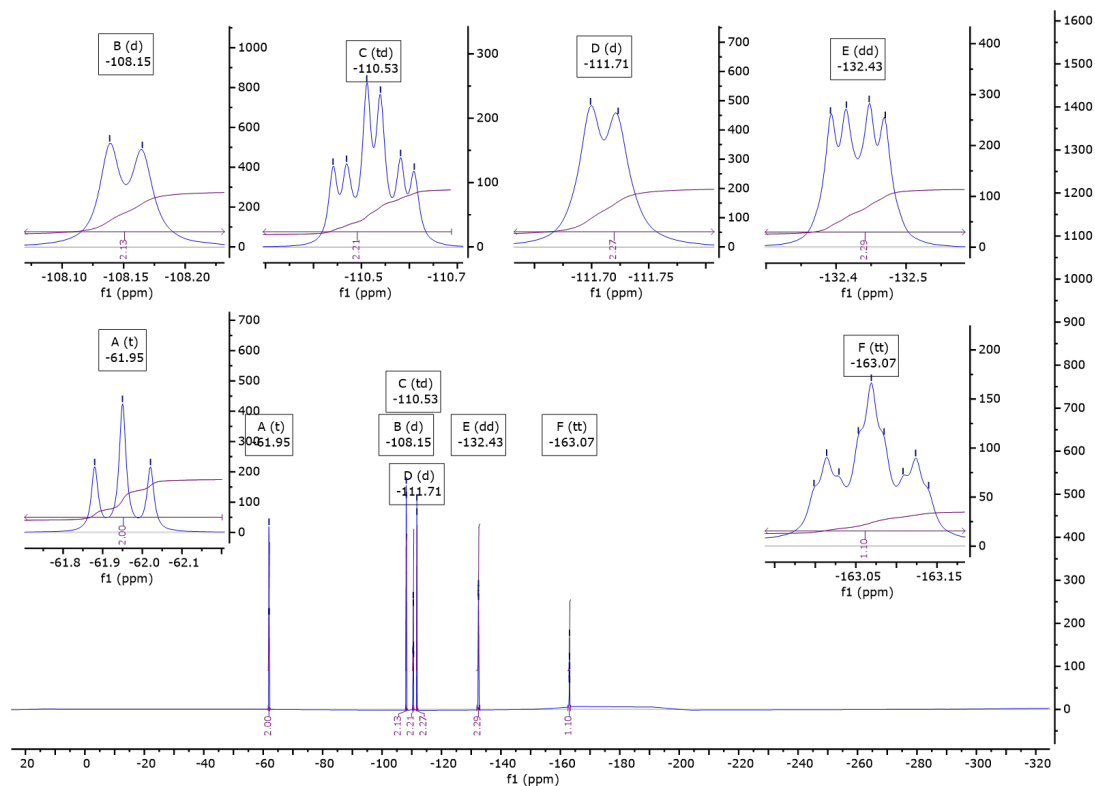
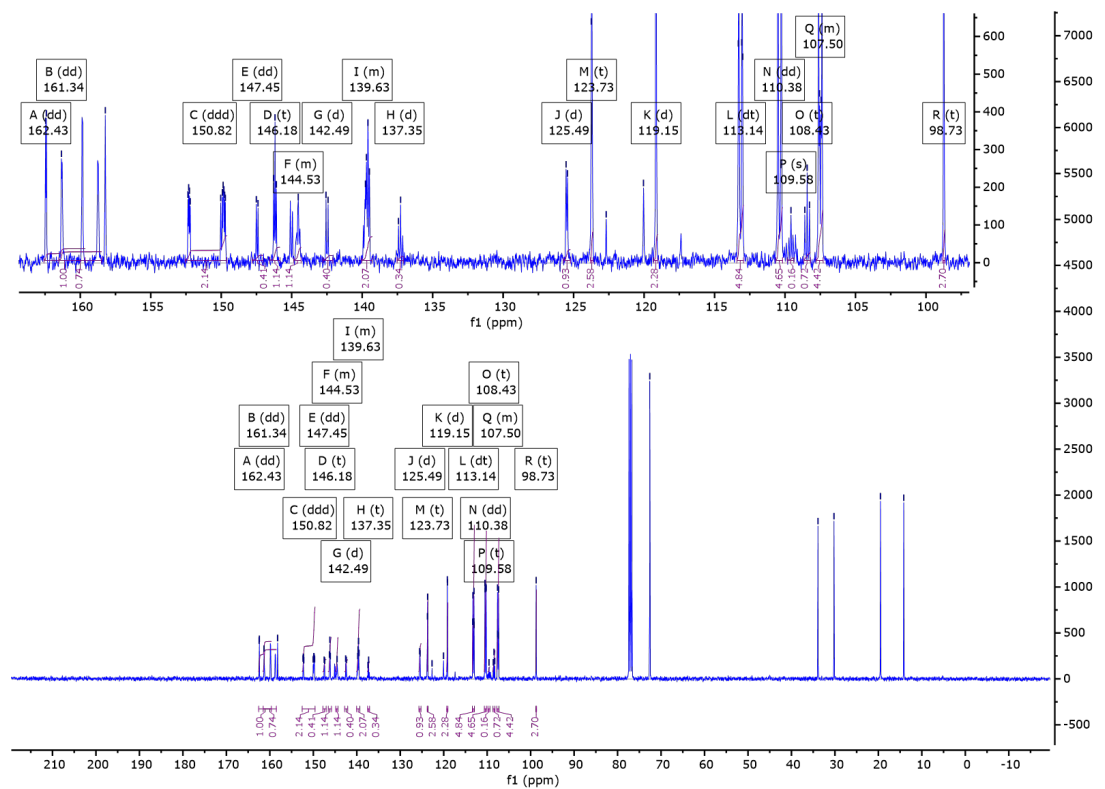
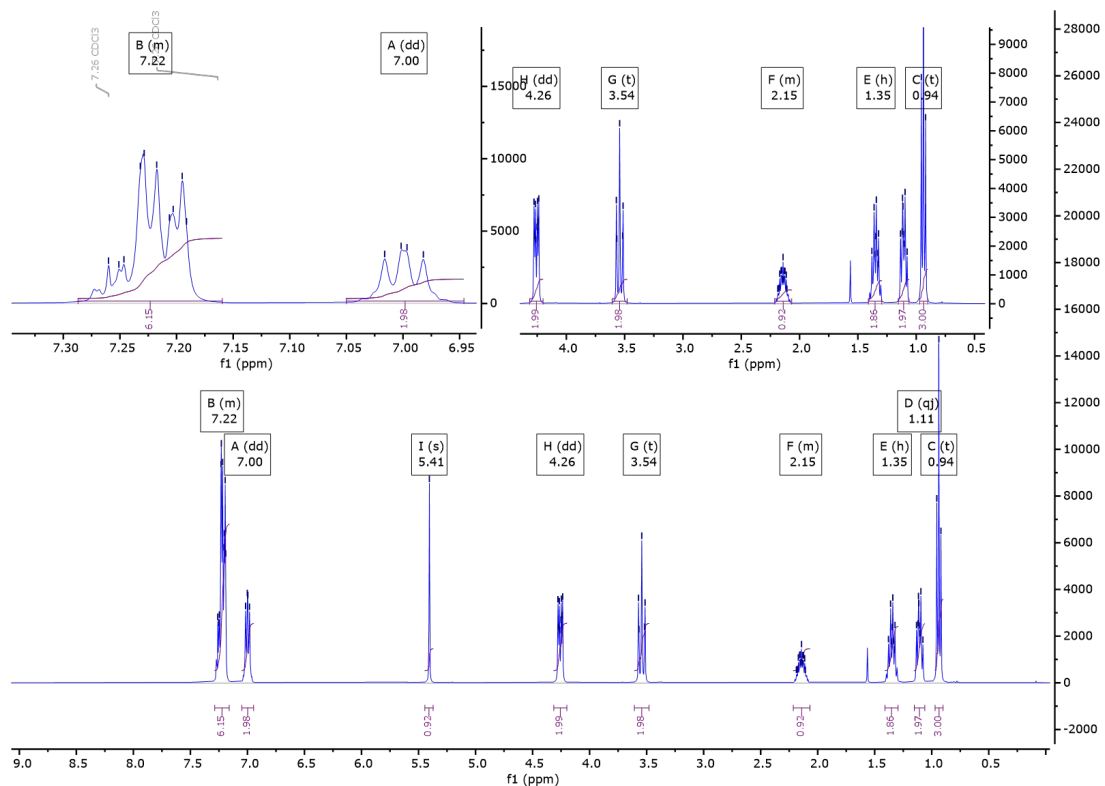


Fig. S15. ^1H [top], $^{13}\text{C}\{^1\text{H}\}$ [middle], and ^{19}F [bottom] NMR spectra, and HRMS Spectra for **3**.



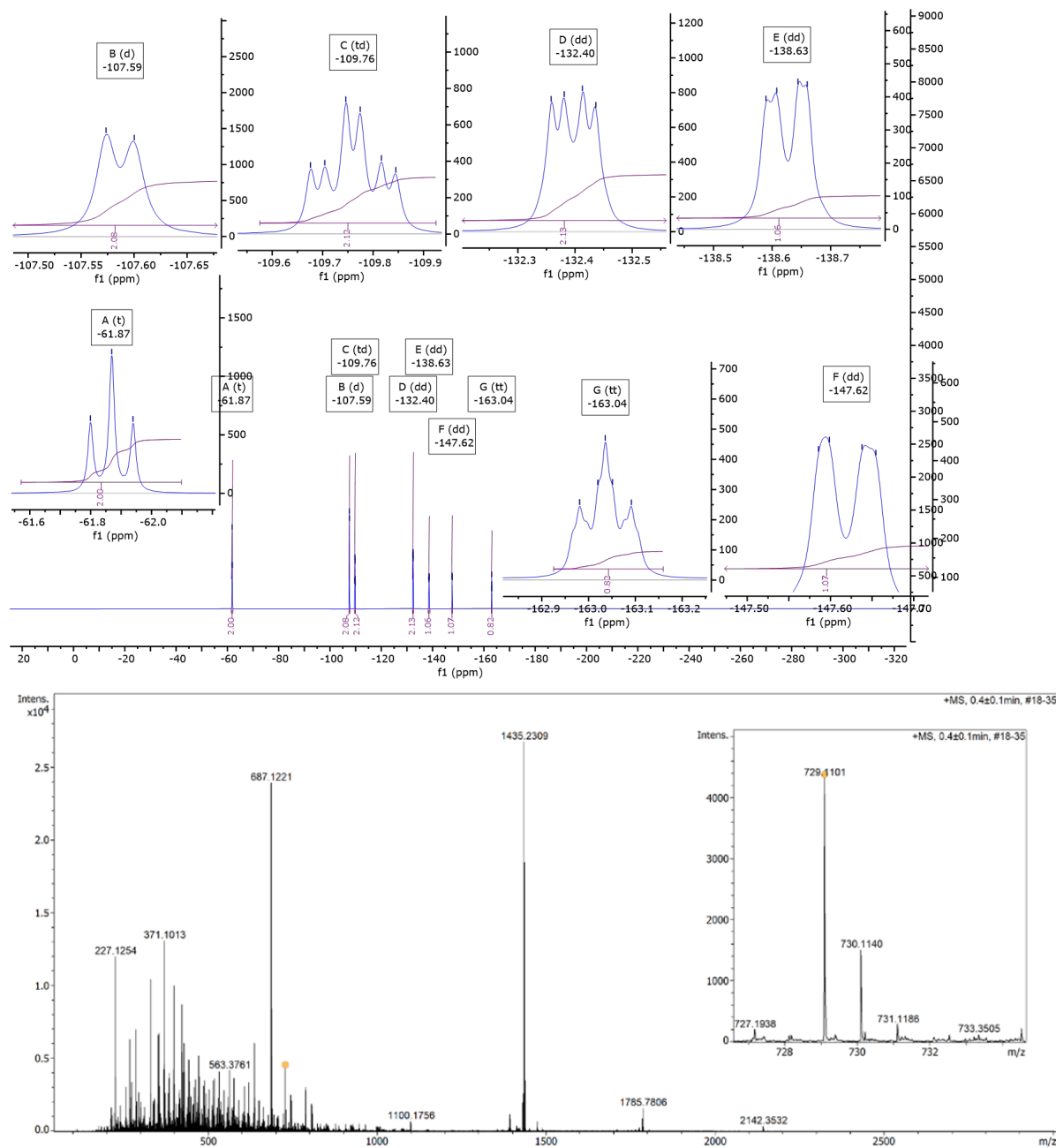


Fig. S16. ^1H [top], $^{13}\text{C}\{^1\text{H}\}$ [middle], and ^{19}F [bottom] NMR spectra, and HRMS Spectra for 4.

4. SUPPLEMENTAL REFERENCES

- [1] Gibb, C.J., Hobbs, J., Nikolova, D.I. et al. Spontaneous symmetry breaking in polar fluids. Nat Commun, 15, 5845 (2024)
- [2] Hobbs, J., Gibb, C.J. and Mandle, R.J. Emergent Antiferroelectric Ordering and the

Coupling of Liquid Crystalline and Polar Order. *Small Sci.*, 4, 2400189 (2024)